

SYNTHESIS AND CHARACTERIZATION OF
Co-Pb/SBA-15 MESOPOROUS CATALYSTS

A THESIS SUBMITTED TO
THE GRADUATE SCHOOL OF NATURAL AND APPLIED SCIENCES
OF
MIDDLE EAST TECHNICAL UNIVERSITY

BY

BURCU AKÇA

IN PARTIAL FULFILLMENT OF THE REQUIREMENTS
FOR
THE DEGREE OF MASTER OF SCIENCE
IN
CHEMICAL ENGINEERING

SEPTEMBER 2006

Approval of the Graduate School of Natural and Applied Science

Prof. Dr. Canan Özgen
Director

I certify that this thesis satisfies all the requirements as a thesis for the degree of Master of Science.

Prof. Dr. Nurcan Baç
Head of Department

This is to certify that we have read this thesis and that in our opinion it is fully adequate, in scope and quality, as a thesis for the degree of Master of Science.

Assist. Prof. Dr. Ayşen Yılmaz
Co-Supervisor

Prof. Dr. Deniz Üner
Supervisor

Examining Committee Members

Prof. Dr. Nurcan Baç (M.E.T.U., Chem. Eng.)

Prof. Dr. Deniz Üner (M.E.T.U., Chem. Eng.)

Assist. Prof. Dr. Ayşen Yılmaz (M.E.T.U., Chemistry)

Prof. Dr. James C.Hill (Iowa State University, Chem.Eng.)

Assist. Prof. Dr. Halil Kalıpçılar (M.E.T.U., Chem. Eng.)

I hereby declare that all information in this document has been obtained and presented in accordance with academic rules and ethical conduct. I also declare that, as required by these rules and conduct, I have fully cited and referenced all material and results that are not original to this work.

Name, Last name : Burcu AKÇA

Signature :

ABSTRACT

SYNTHESIS AND CHARACTERIZATION OF Co-Pb/SBA-15 MESOPOROUS CATALYSTS

Akça, Burcu

M.S., Department of Chemical Engineering

Supervisor: Prof. Dr. Deniz Üner

Co-Supervisor: Assist. Prof. Dr. Ayşen Yılmaz

September 2006, 75 Pages

Co and Pb are soft oxides, making them useful in partial oxidation catalysis. But it is difficult to prepare high surface area, nanometer size particles due to the low melting point of Pb. In the present study, SBA-15 samples are incorporated with Co and/or Pb at different weight loadings to provide a controlled geometry in nanometer scale via using direct synthesis method. The characterization of the synthesized samples was done by XRD, N₂ adsorption isotherms, TEM images and XPS analysis. The increase in the metal loading in SBA-15 causes a decrease in the BET surface area due to the filling of pores with metal atoms. No characteristic peaks of metal oxide was observed up to 15 wt %Pb loading into SBA-15 in the large angle XRD pattern indicating that metal particles are dispersed in the SiO₂ structure without accumulating and forming crystals. However, 20 wt%Pb loaded SBA-15 showed more appreciable characteristic peaks, indicating appreciable quantities of crystallites of metal oxide on the surface of silica. The introduction of high amount of cobalt and lead oxides to SBA-15 resulted in the loss of long range order of pores according to the low angle XRD patterns. The hexagonal structure of pores of SBA-15 was

confirmed by TEM images for all samples. XPS analysis indicated that binding energies of O 1s and Si 2p are almost similar in Co or Pb loaded samples, while mixed oxide loaded samples showed slightly higher binding energies which means the structure grows into a different type.

KEYWORDS: Mesoporous materials, SBA-15, Lead, Cobalt, Catalyst

ÖZ

Co-Pb/SBA-15 MEZOGÖZENEKLİ KATALİZÖRLERİN SENTEZ VE KARAKTERİZASYONU

Akça, Burcu

Y.Lisans, Kimya Mühendisliği Bölümü

Tez Yöneticisi: Prof. Dr. Deniz Üner

Ortak Tez Yöneticisi: Yrd. Doç. Dr. Ayşen Yılmaz

Eylül 2006, 75 Sayfa

Co ve Pb, kısmi oksidasyon katalizinde kullanılan yumuşak oksitlerdir. Fakat kurşunun düşük erime sıcaklığından dolayı yüksek yüzey alanına sahip, nanometre boyutunda partiküller hazırlamak zordur. Bu çalışmada, direkt sentez yöntemi ile nanometre boyutunda kontrol edilebilir bir geometri sağlamak için SBA-15 (Santa Barbara No :15) örnekleri değişik ağırlık yüzdelerinde Co ve/veya Pb eklenerek geliştirilmiştir. Sentezlenen örneklerin karakterizasyonları XRD, BET, TEM ve XPS analizleri ile yapılmıştır. SBA-15'e eklenen metallerin artması, gözeneklerin metal atomları ile dolmasından dolayı BET yüzey alanının düşmesine neden olmuştur. Geniş açılı XRD grafiklerinde, SBA-15'e ağırlıkça %15' e kadar Pb eklenmesi ile hiçbir metal oksit pikine rastlanmamış olması metal partiküllerinin SiO₂ yapısı içinde topaklanmadan ve kristaller oluşturmadan dağılmış olduğunu göstermektedir. Fakat, SBA-15 içine ağırlıkça %20 Pb eklenmesi ile daha karakteristik pikler görülmesi, silika yüzeyinde metal oksit kristallerinin oluştuğunu göstermektedir. Düşük açılı XRD grafiklerine göre, SBA-15 içine yüksek miktarlarda kobalt ve kurşun eklenmesi uzun ve düzenli gözenek yapısının bozulmasına neden olmuştur. TEM görüntüleri ile tüm örnekler için SBA-15 gözeneklerinin altıgen yapıda olduğu doğrulanmıştır. XPS analizi, Co veya Pb eklenmiş örneklerde O 1s ve Si 2p'nin bağlanma enerjilerinin

hemen hemen aynı olduđu gösterirken, karışık oksit eklenmiş örnekler daha yüksek bağlanma enerjisi göstererek yapının deđiştini ortaya koymuştur.

ANAHTAR KELİMELER : Mezogözenekli malzemeler, SBA-15, Kurşun, Kobalt, Katalizör

To My Father

ACKNOWLEDGEMENTS

I would like to thank every person who has encouraged me throughout the research, firstly my family and my supervisors Prof. Dr. Deniz Üner and Ass. Prof. Dr. Ayşen Yılmaz for their supervision and patience during my study.

I also would like to thank Mukaddes Can for her contributions and support during my research. I'm also grateful to Semih Seyyidođlu, Mustafa Fatih Genişel, Ebubekir Şen from METU Chemistry Department and Selda Keskin from METU Central Laboratory for their technical assistance.

I also want to express my gratitude to Gülten Orakçı, Mihrican Açıkğöz and Kerime Güney from Chemical Engineering Department for their technical support in BET, TGA-DSC and AAS measurements respectively.

I want to extend my thanks to Galen Stucky group of UC Santa Barbara for their assistance in TEM measurements.

I would also like to express my appreciation to whole Cactus Research Group (Ebru Erünal, Volkan Değirmenci, Hilal Demir, Orçun Erođlu, Arzu Kanca, Özge Güner, Hakan Ö. Olcay, Özlem Özcan, Volkan E. Genç, Bora Atalık and other members) and others whom I forgot to mention.

TABLE OF CONTENTS

PLAGIARISM.....	iii
ABSTRACT.....	iv
ÖZ.....	vi
ACKNOWLEDGMENTS.....	ix
TABLE OF CONTENTS.....	x
CHAPTERS	
1. INTRODUCTION.....	1
2. LITERATURE SURVEY.....	6
2.1 Mesoporous Materials.....	6
2.2 Types of Mesoporous Materials.....	8
2.3 Surfactants for the Synthesis of Mesoporous Materials.....	8
2.4 Usage of Mesoporous Materials in Catalysis.....	10
2.5 Ways for the Functionalization of the Catalysts.....	11
2.6 SBA-15 (Santa Barbara No. 15).....	13
2.7 Oxygen Adsorption Properties of Co/Pb Catalysts.....	14
3. THEORY.....	17
4. EXPERIMENTAL.....	21
4.1 Catalyst Preparation	
4.1.1 Synthesis of Mesoporous SBA-15 Silica.....	22
4.1.2 Synthesis of Co/ SBA-15, Pb/SBA-15 and Co/Pb/SBA-15.....	22
4.2 Catalyst Characterization.....	22
4.2.1 X-Ray Diffraction Analysis.....	22
4.2.2 BET Surface Analysis.....	23
4.2.3 Thermo Gravimetical Analysis.....	23
4.2.4 Differential Scanning Calorimeter Analysis.....	23
4.2.5 TEM Analysis.....	23
4.2.6 AAS Analysis.....	24
4.2.7 XPS Analysis.....	24

5. RESULTS & DISCUSSION.....	25
5.1 X-ray Diffraction Analysis.....	25
5.2 BET Surface Area Measurements.....	31
5.3 Thermal Analysis by TGA/DSC	33
5.4 TEM Analysis	34
5.5. Quantitative Analysis by AAS.....	37
5.6 XPS Analysis	38
6. CONCLUSION	44
REFERENCES.....	46
APPENDICES	
Appendix A: Physical and Thermodynamic Properties of Pb and Co Oxides.....	49
Appendix B: Equilibrium Conversion Calculations	52
Appendix C: Co and/or Pb Incorporated SBA-15 Samples Synthesized	63
Appendix D: d-values for the Metal Loaded Samples.....	64
Appendix E: TGA and DSC Results.....	70

LIST OF TABLES

Table 1.1. Typical Emissions of Combustion Processes.....	3
Table 1.2. EU Emission Standards for Diesel Passenger Cars	4
Table 3.1. Thermodynamic Properties of the Components.....	18
Table 5.1. 2θ angles for the peaks of Pb loaded SBA-15	27
Table 5.2. 2θ angles for the peaks of Co loaded SBA-15.....	29
Table 5.3. The mixed oxide catalyst compositions and surface areas	33
Table 5.4. Lead Content of the Samples	38
Table 5.5. Binding Energies of Co 2p and Pb 4f levels for Pb or Co and Pb-Co loaded SBA-15 samples	40
Table 5.6. Binding Energies of O 1s and Si 2p levels for Pb or Co and Pb-Co loaded SBA-15 samples.....	43

LIST OF FIGURES

Figure 2.1 Three structure types for silica-surfactant mesophases	7
Figure 2.2 Schematic sketch of the various methods for the functionalization of mesoporous material.....	12
Figure 2.3. Formation of the triblock copolymer/mesostructured silica and mesoporous silica SBA-15	14
Figure 3.1 Equilibrium Conversion versus Temperature Graph for BaO, CoO and PbO	20
Figure 5.1 Wide angle XRD patterns of Pb/SBA-15	26
Figure 5.2 Low angle XRD patterns of Pb/SBA-15	27
Figure 5.3 Wide angle XRD patterns of Co/SBA-15.....	28
Figure 5.4. Low angle XRD patters for Co/SBA-15.....	29
Figure 5.5 Wide angle XRD patterns for Co-Pb/SBA-15.....	30
Figure 5.6. Low angle XRD patterns of Co-Pb/SBA-15	31
Figure 5.7. Nitrogen adsorption-desorption isotherms for the mesoporous silicas	32
Figure 5.8 TEM images of pure SBA-15	34
Figure 5.9 TEM image of 5%Pb 55%Si	35
Figure 5.10 TEM images of 20%Pb 55%Si.....	35
Figure 5.11 TEM image of 10%Co 40%Si.....	36
Figure 5.12 TEM images of 40%Co 40%Si.....	36
Figure 5.13 TEM image of 17%Pb 40%Co 15%Si	37
Figure 5.14 TEM images of 10%Co 25%Pb 40%Si.....	37
Figure 5.15 XPS Spectra of Pb 4f levels for 20%Pb 55%Si catalyst.....	39
Figure 5.16 XPS Spectra of Co 2p levels for 40%Co 40%Si catalyst.....	40
Figure 5.17 XPS Spectra of Pb 4f levels for Pb/SBA-15 and Co-Pb/SBA-15 samples.	41
Figure 5.18 XPS Spectra of Co 2p levels for Co/SBA-15 and Co-Pb/SBA-15 samples	41
Figure 5.19 XPS profiles of O1s for different metal loaded catalysts	42
Figure 5.20 XPS profiles of Si 2p for different metal loaded catalysts	42

CHAPTER I

INTRODUCTION

Otto and Diesel engines are the most common types of internal combustion engines. Diesel engine, a type of internal combustion engine, was developed by Rudolf Diesel in 1892 with a goal to create an engine with high efficiency. Gasoline engines had been invented in 1876 and, especially at that time, were not very efficient.

There exists some main differences between the gasoline engine and the Diesel engine. In terms of working principle, gasoline engine intakes a mixture of gas and air, compresses it and ignites the mixture with a spark while Diesel engine takes in just air, compresses it and then injects fuel into the compressed air. The heat of the compressed air lights the fuel spontaneously. A gasoline engine compresses at a ratio of 8:1 to 12:1, while a Diesel engine compresses at a ratio of 14:1 to as high as 25:1. The higher compression ratio of the diesel engine leads to better efficiency. Gasoline engines generally use either carburetion, in which the air and fuel is mixed long before the air enters the cylinder, or port fuel injection, in which the fuel is injected just prior to the intake stroke (outside the cylinder). Diesel engines use direct fuel injection which means that the Diesel fuel is injected directly into the cylinder [1].

1.1. Diesel Fuel versus Gasoline

There are some distinctions between Diesel fuel and gasoline when compared. Diesel fuel is heavier and oilier and it evaporates much more slowly than gasoline. It contains more carbon atoms in longer chains than gasoline does. The molecular formula of gasoline is typically C_9H_{20} , while the molecular formula of Diesel fuel is typically $C_{14}H_{30}$. Due to the fact that it takes less refining to create Diesel fuel, it is generally cheaper than gasoline. Diesel fuel has a higher energy density than

gasoline. This, combined with the improved efficiency of diesel engines, explains why Diesel engines get better mileage than equivalent gasoline engines [1].

1.2 Exhaust Emissions and Aftertreatment Techniques

The Diesel exhaust contains principally three primary pollutants, unburned or partially burned hydrocarbons (HCs), carbon monoxide (CO) and nitrogen oxides (NO_x), mostly NO, as well as particulate matter (PM) in addition to other compounds such as water, hydrogen, nitrogen and oxygen [2].

In the USA, in 1994, on-road vehicles were reported to contribute 62 percent of CO emissions, 42 percent of HC emissions, 32 percent of NO_x emissions, ~5 percent of SO₂, 19 percent of PM-10, and 28 percent of Pb [3].

Since there are strict regulations for the emission values, research for reducing the emissions gains importance. In the scope of these studies, after-treatment techniques by using catalytic converters gained more attention in the early 1980s. The catalytic converters treated exhaust gas successfully by removing much of the CO, HC and NO_x in the gasoline vehicles [3]. Three-way catalyst technology can be applied in gasoline engine operation under stoichiometric conditions. It is possible to operate the gasoline engine under lean-burn conditions and this provides some fuel economy benefit. However, the three-way catalyst is not able to reduce NO_x when running lean. In the presence of excess oxygen in the exhaust gas, NO_x can not be removed by Three Way Catalytic Converters (TWC) [4].

The pollutant gases emitted from Diesel and Otto engines are reported in Table 1.1. The effect of the introduction of TWC decreasing the emissions for gasoline engine is obviously seen.

Table 1.1 Typical Emissions of Combustion Processes (g/kg fuel) [5]

	CO	HC	NO _x	SO _x	Particulate
Diesel Engine	3-30	0.5-10	5-20	0.5-5	1-10
Otto Engine	20-200	10-50	10-60	0.1-1	0.1-0.4
Otto Engine+TWC	2-30	0.5-5	0.2-4	0.1-1	0.05-0.3

1.3 Health Effects

Vehicles are important sources of air pollution with pollutants including oxides of nitrogen (NO_x), carbon monoxide (CO) and particulate matter (PM). Studies have indicated a correlation between the exposure to exhaust emissions and increased respiratory symptoms, hospitalization for respiratory diseases and premature mortality among general population [6].

1.4 Regulations

Emissions are subject to strict regulations worldwide, since they are harmful for both environment and human health. Despite diesel engines have a good fuel economy, emissions contain other compounds that may also pose a health threat to humans, including polynuclear aromatic hydrocarbons (PAHs), nitro-PAHs, aldehydes, and other hydrocarbons and their derivatives besides CO, HC, NO_x and PM [7]. Lean fuel mixtures (high A/F ratios) will typically produce higher amounts of NO_x (especially during very hot, lean conditions) and lower amounts of CO and HC because combustion is more complete [3]. Emission standards adopted by European Union for passenger cars and light commercial vehicles are summarized in Table 1.2.

Table 1.2 EU Emission Standards for Diesel Passenger Cars, g/km [8]

	EURO I (1992)		EURO II (1996)		EURO III (2000)		EURO IV(2005)	
	Diesel	Gasoline	Diesel	Gasoline	Diesel	Gasoline	Diesel	Gasoline
CO	2.72	2.72	1.0	2.2	0.64	2.3	0.5	1.0
HC	-	-	-	-	-	0.2	-	0.1
NO _x	-	-	-	-	0.50	0.15	0.25	0.08
PM	0.14	-	0.1	-	0.05	-	0.025	-

1.5 NO_x Emissions

Nitrogen oxides or NO_x is the generic term for a group of highly reactive gases, all of which contain nitrogen and oxygen in varying amounts [3]. Nitrogen monoxide (NO) accounts for 95% of all nitrogen oxide emissions [9]. Nitrogen oxides form when fuel is burned at high temperatures, as in a combustion process. The primary manmade sources of NO_x are motor vehicles, electric utilities, and other industrial, commercial, and residential sources that burn fuels [3].

NO_x causes a wide variety of health and environmental impacts because of various compounds and derivatives in the family of nitrogen oxides, including nitrogen dioxide, nitric acid, nitrous oxide, nitrates, and nitric oxide. NO_x leads to the formation of ground-level ozone when NO_x and volatile organic compounds (VOCs) react in the presence of sunlight [3].

1.6 NO_x Abatement

Abatement of dilute NO_x in the exhaust gas from lean-burn and diesel engines is of great concern, since in spite of the application of the two established catalytic DeNO_x technologies, NH₃-SCR (selective catalytic reduction) and TWC (three-way catalyst), the NO_x concentration in the atmosphere is still high. Reduction of NO_x with hydrocarbons (HC-SCR) is a promising catalytic technology and much effort has been devoted to this subject. However, there remains several serious problems to be solved [10]. Another method is NO_x storage and reduction (NSR) that is capable of reducing NO_x in excess oxygen. As NO_x storage component, several metal oxides (mainly alkaline earth metal oxides) have proven effective in forming nitrates with NO₂. Examples of such metals are barium and strontium[11].

In a recent study, it was presented that an advanced HC-SCR type of mesoporous catalysts, which mean the HC-SCR catalysts supported on mesoporous materials, to effectively achieve de-NO_x of the lean-burn emissions. Platinum catalysts supported on the mesoporous silica and metal substituted silicates established high NO-conversions. The de-NO_x properties of the HC-SCR mesoporous catalysts were compared with those for a typical NO_x-storage–reduction-catalyst. The new catalysts, which basically consist of mesoporous silica or metal-substituted silicates for supports and platinum for catalytically active species, were found to be very useful and stable for cleaning lean-burn NO_x emissions and alternative to the conventional NO_x-absorption–reduction-catalysts [12].

CHAPTER II

LITERATURE SURVEY

2.1 Mesoporous Materials

Mesoporous materials are one of the types of porous materials with pore diameters in the range of 2-50 nanometers. The mesoporous silicas are made up of frameworks (pore walls) which are crystallographically amorphous [13]. These materials are special types of nanomaterials with ordered arrays of uniform nanochannels. They have important applications in a wide variety of fields such as separation, catalysis, adsorption and advanced nanomaterials [14]. These mesoporous materials exhibit high surface area (600–1300 m²/g), and large pore size exhibiting widely potential applications in industrial catalytic reactions [15 and references therein].

Indeed, these ordered mesoporous solids discovered in 1992 having regular, well-defined, and uniform channels are displaying both the molecular sieving properties of zeolites (with much larger pores than the usual microporous aluminosilicates) and the chemical reactivity of the amorphous silica surface (e.g., they can be covalently grafted with organic groups, or their organic–inorganic hybrid forms can be prepared in one-step according to the sol-gel process in the presence of a structure-directing agent) [16 and references therein].

Since the discovery of the hexagonal mesoporous materials (M41S family by Beck and coworkers [21], SBA-15 by Stucky and coworkers [22]) considerable efforts have been made to understand their structure and control their morphology in terms of pore size (in the range 3–30 nm), wall thickness (in the range 1–4 nm) and texture (in micron or even millimeter range of particle size). All these properties are

extremely important for the potential application of these materials [17 and references therein].

The first synthesis of an ordered mesoporous material was described in the patent literature in 1969. However, due to a lack of analysis, the remarkable features of this product were not recognized. In 1992, a similar material was obtained by scientists in Mobil Oil Corporation who discovered the remarkable features of this novel type of silica and opened up a whole field of research. MCM-41, which stands for Mobil Composition of Matter No. 41, shows a highly ordered hexagonal array of unidimensional pores with a very narrow pore size distribution. The walls, however, very much resemble amorphous silica. Other related phases such as MCM-48 and MCM-50, which have a cubic and lamellar mesostructure, respectively, were reported in these early publications as well [18 and references therein].

Pure silica mesoporous molecular sieves exhibit three structure types: hexagonal (1D regular hexagonal packing of mesopore channels), cubic (3D bicontinuous system of pores), and lamellar (2D system of silica sheets interleaved by surfactant bilayers), as illustrated in Fig. 2.1.

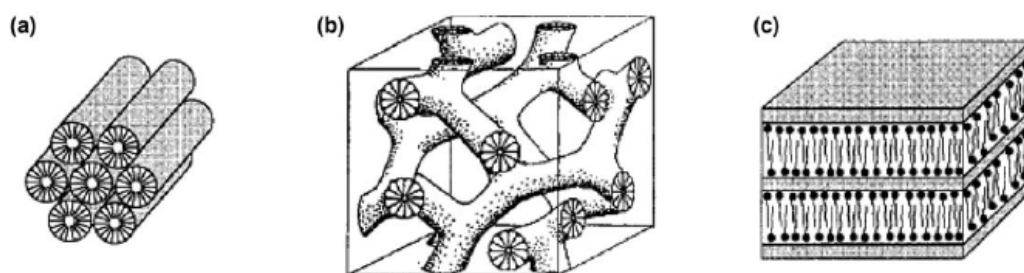


Figure 2.1 Three structure types for silica-surfactant mesophases; (a)hexagonal; (b) cubic bi-continuous; (c) lamellar [16]

2.2 Types of Mesoporous Materials

There exist three kinds of relevant materials obtained following different synthetic procedures. The first one is so-called M41S family of silica and aluminosilicates introduced by the Mobil group which includes hexagonal MCM-41, cubic MCM-48 and lamellar MCM-50 phases.

The second one was introduced by the group of Pinnavaia who produced MMS (Mesoporous Molecular Sieves) using two neutral routes based on hydrogen bonding and self assembly of non-ionic primary amines such as hexadecyl amine or polyethylene oxide (EO) surfactants and neutral oligomeric silica precursors S^{0I^0} . The hexagonal mesoporous silica (HMS and MSU) produced by this technique are less ordered, showing a wormhole like pore structure, than MMS's produced with ionic surfactants. They have, however, a monodispersed pore diameter, thicker pore walls, a higher degree of condensation, and therefore, a higher thermal stability. In addition, the mesopores of HMS being shorter allow a faster diffusion of reactants.

Finally, Stucky and co-workers introduced a new synthesis route involving amphiphilic di- and tri-block copolymers as organic structure directing agents. These materials, exemplified by hexagonal SBA-15, have long range order, large monodispersed mesopores (up to 50 nm) and thicker walls (typically between 3 and 9 nm) which make them more thermally and hydrothermally stable than previous materials. One of the advantages of the thicker walls is the ability to form stable crystal nuclei of the constitutive oxide within the walls [19 and references therein].

2.3 Surfactants for the Synthesis of Mesoporous Materials

Previous work on the synthesis of mesoporous silica molecular sieves has revealed that the mesopore diameters can be controlled by using surfactants with different tail

lengths, polymer as templates, suitable organic additives, such as 1,3,5-trimethylbenzene, triisopropylbenzene, alkanes, amines and tetraalkylammonium cations, and also by the hydrothermal post-synthesis treatment. [20 and references therein].

While the early work on mesoporous templating focused on ionic surfactants as the templating agent, subsequent work has shown that nonionic surfactants and block copolymers can also be used to form mesoporous materials [21]. Nonionic alkyl poly(oxyethylene) surfactants and poly(oxyalkylene) block copolymers are important families of surfactants that are widely used. They display excellent interfacial stabilization properties and are low-cost, nontoxic, and biodegradable. Block copolymers have the advantage that their ordering properties can be nearly continuously tuned by adjusting solvent composition, molecular weight, or copolymer architecture [22].

One of the most useful groups of surfactants are the triblock co-polymers consisting of poly(ethylene oxide)_x – poly(propylene oxide)_y – poly(ethylene oxide)_x, (PEO)_x(PPO)_y(PEO)_x, (trade name: Pluronics) which show the ability to form liquid-crystal structures. They can be used to synthesize a variety of different ordered mesoporous materials with rather large pores in various framework compositions under strongly acidic conditions [18 and references therein].

Similar to, zeolite syntheses, organic molecules—surfactants function as templates forming an ordered organic inorganic composite material. Via calcination the surfactant is removed, leaving the porous silicate network [23 and references therein].

2.4 Usage of Mesoporous Materials in Catalysis

Mesoporous materials have several possible applications within heterogeneous catalysis, due to their high surface area and ordered pore structure [24].

The advantage of using ordered mesoporous solids in catalysis are the relatively large pores which facilitate mass transfer and the very high surface area which allows a high concentration of active sites per mass of material. In recent years, environmental and economic considerations have raised strong interest to redesign commercially important processes so that the use of harmful substances and the generation of toxic waste could be avoided. In this respect, heterogeneous catalysis can play a key role in the development of environmentally benign processes in petroleum chemistry and in the production of chemicals [18].

The amorphous pore walls give mesoporous silicas a great deal of flexibility in terms of their composition and pore channel structure and allow post-synthesis modifications which may be performed for pore size control framework stabilisation, compositional modifications or the formation of mesoporous/zeolite composite materials [25 and references therein].

But unfortunately, these mesoporous materials have relatively low catalytic activity and hydrothermal stability, which severely hinders their practical applications in catalysis. The relatively low catalytical activities of mesoporous materials such as can be typically attributed to the low acidity or low oxidation ability of catalytically active species, which is strongly related to the amorphous nature of the pore walls. Therefore, increasing acidity, oxidation ability, and hydrothermal stability are great tasks for rational syntheses of ordered mesoporous materials [15 and references therein].

2.5 Ways for the Functionalization of the Catalysts

Mesoporous silica materials are not catalytically active by themselves. These materials therefore have to be functionalized in some way for application as catalysts.

As summarized in [24], “there are several different procedures that are applied to functionalize catalysts and two of the most commonly used for mesoporous materials are direct functionalization by metal incorporation and incipient wetness impregnation [18]. The direct method is a “one-pot” procedure, where the metal precursors are added during synthesis and are incorporated into the framework. This one-step procedure is relatively simple, and it is also possible to control the pore size, pore structure, and metal amount during synthesis. However, the framework becomes less thermally stable due to the incorporated metals [25], and since the wall thickness of mesoporous materials is about 1 nm, a significant portion of the incorporated metals will be located inside the walls and thus inaccessible as catalytically active sites. Incipient wetness impregnation is a widely used functionalization method for preparation of supported catalysts and is also applied industrially. In this postsynthesis procedure, a metal salt solution is added to the support in an amount to exactly fill the pore volume, and the material is then dried and calcined [26]. This procedure is simple; however, a large portion of the precipitated particles ends up outside the pore system of the support. Some of the advantages of having a mesoporous support with an ordered and well-defined pore structure may therefore be lost if the active particles are located at the external surface. Incipient wetness impregnation may therefore not be so suited for functionalization of mesoporous materials, at least not for model studies.”

While the direct method typically will result in a relatively homogeneous incorporation of the heteroelement, post-synthesis treatment will primarily modify

the wall surface and thus lead to increased concentration of the heteroelement on the surface [18].

The possible pathways to modify mesoporous materials to give them a new catalytic function is schematically shown in Fig. 2.2.

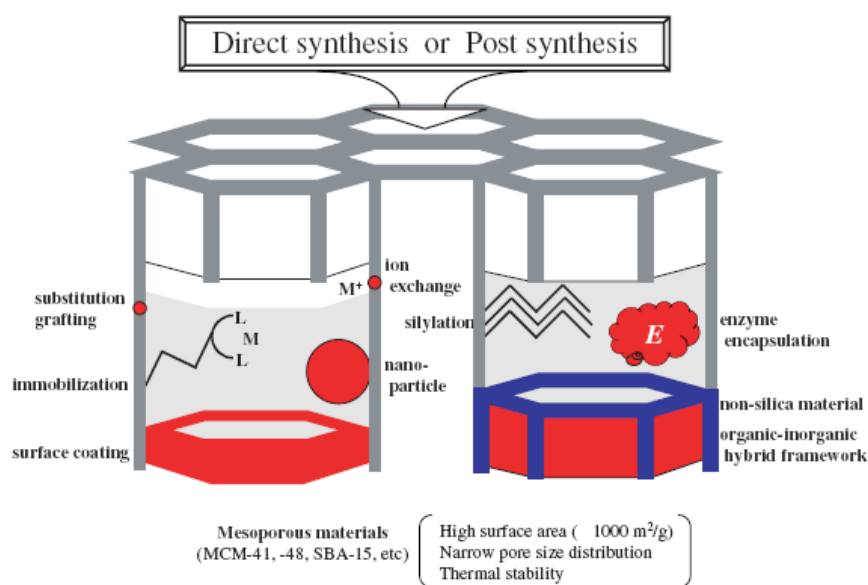


Figure 2.2 Schematic sketch of the various methods for the functionalization of mesoporous material [18]

In order to modify the catalytic activity of the mesoporous materials, especially to create active sites, several other metal ions were incorporated into the silica framework or grafted on the surface (titanium, zirconium, iron, cobalt, platinum, etc.). Compared to other support materials, the ordered mesoporous solids have the advantage of stabilizing metal or metal oxide particles, since they cannot grow to sizes larger than the pore size unless they move to the external surface of the particles [18].

Even though many applications do not require high temperatures, the hydrothermal stability of the catalyst is still critical for such classical catalytic processes as cracking or hydrotreatment. Hydrolysis of the Si–O–Si bridges leads to the pore lattice collapse. Therefore, structural stability is dependent on the level of condensation in walls (related to wall thickness) and to the surface density of silanol groups. This explains why thicker wall materials such as those synthesized using triblock copolymers as surfactants, exemplified by SBA-15, are more stable than M-41S solids [19].

2.6 SBA-15 (Santa Barbara No. 15)

SBA-15 is by far the largest pore-size mesoporous material with highly ordered hexagonally arranged mesochannels. SBA-15, which possesses larger pores, thicker walls and higher thermal and hydrothermal stability as compared with other mesoporous silicas may be used as a promising catalyst support, particularly for reactions occurring at high temperatures [27 and references therein].

SBA-15, with uniform tubular channels is one of the most widely studied mesoporous silica. It can be readily prepared over a wide range of uniform pore size (4.6–30 nm) and pore wall thickness (3.1–6.4 nm), by using a variety of poly(ethylene oxide)–poly(propylene oxide)–poly(ethylene oxide) triblock copolymers ($\text{EO}_x\text{PO}_y\text{EO}_x$) as templates, as shown in Fig. 2.3 [28].

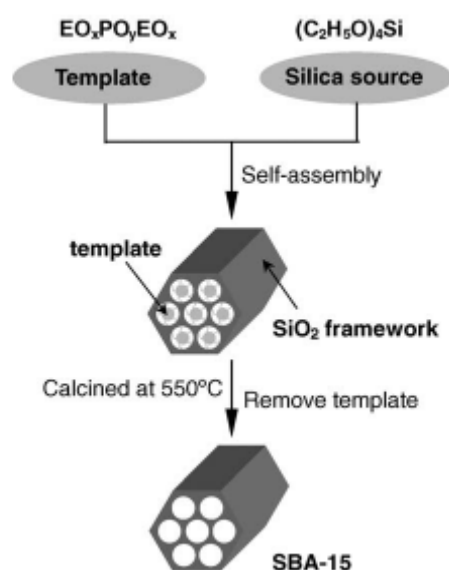


Figure 2.3. Formation of the triblock copolymer/mesoporous silica and mesoporous silica SBA-15 [28]

The 2D hexagonal mesoporous material formed via this pathway has thicker walls. The thick wall of this material significantly improves the thermal and hydrothermal stability compared to mesoporous MCM-41 and related silicas [18].

2.7 Oxygen Adsorption Properties of Co/Pb Catalysts

Recently, there are various studies in which Pb and Co are being used in different applications. One of the studies was performed by Cattarin et al. [29] for oxygen evolution by electrodeposition of composite Pb and Co oxides. The simultaneous anodic oxidation of Pb^{2+} and Co^{2+} in a sulphamate bath containing suspended Co_3O_4 (or $NiCo_2O_4$) particles has been studied as a method for preparing composite oxides in which the particles are dispersed in a matrix consisting of PbO_2 and hydrous Co oxides, CoO_x with $X < 2$. The $(PbO_2 + CoO_x) + Co_3O_4$ composites are more active

catalysts in the oxygen evolution reaction than either $\text{PbO}_2+\text{CoO}_x$ or $\text{PbO}_2+\text{Co}_3\text{O}_4$. The electrodeposition of oxide-matrix composites as a way for producing anodes for the oxygen evolution reaction (o.e.r.) exhibits satisfactory activity and stability. Compared to $\text{PbO}_2 + \text{Co}_3\text{O}_4$ or $\text{PbO}_2 +\text{CoO}_x$ anodes, the materials prepared in this work exhibit much higher initial catalytic activity.

In another study carried out by Casellato et al. [30], porous PbO_2 electrodes by electrochemical deposition of composites were prepared. The electrodeposition of composites is a subject of both scientific and industrial interest, which is expanding from its original functional coatings domain to the preparation of a variety of materials. The anodic electrodeposition of a composite material in which both the matrix and the dispersed phase are PbO_2 , aimed at obtaining deposits of high surface roughness (surface roughness is defined as the ratio between the true and the apparent surface area). When the electrocatalysts of oxygen evolution on PbO_2 -matrix composites containing either Co_3O_4 or RuO_2 were studied, the main reason for their increased activity was to be found in a change in the reaction mechanism.(i.e. a true catalytic action of the incorporated particles.) Porous PbO_2 electrodes prepared by codeposition might be interesting materials for the oxidative degradation of organic pollutants.

Petrova et al. [31], investigated the electrochemical behaviour of lead alloys as anodes in zinc electrowinning. The electrochemical and corrosion properties of the ternary and quaternary lead alloys Pb-Ag-Co and Pb-Ag-Sn-Co have been investigated. Lead-cobalt alloys are the only convenient materials owing to their high corrosion resistance and the fact that they eliminate the hazards of impurity inclusion. The inclusion of cobalt in lead strongly inhibits the $\text{Pb} \rightarrow \text{PbO}_2$ oxidation reaction, reduce the anodic polarization and improve the corrosion resistance of the alloy.

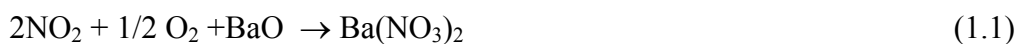
In another research of Quiroz et al. [32], electrocatalytic oxidation of p-nitrophenol from aqueous solutions at Pb/PbO₂ anodes was investigated. Nitroaromatic compounds formed by photochemical atmospheric reactions owing to the presence of nitrogen oxides (NO_x) have been detected not only in industrial wastewaters but also in freshwater and marine environments. In particular, p-nitrophenol (p-NPh), a toxic insecticide is also present in wastewaters from industries such as refineries. The presence of a nitro-group confers to the aromatic compound a strong chemical stability. The electrocatalytic activity of PbO₂ towards p-NPh anodic oxidation has been evaluated in acidic and alkaline media. Lead dioxide (PbO₂) was chosen as the electrocatalyst for the reasons that it allows an efficient degradation of phenol, it can be easily prepared by anodic polarization of lead metal in acidic media and it can be doped with metallic cations to produce anodes having a lower corrosion rate. Pb/PbO₂ anodes exhibit good electrocatalytic properties towards the oxidation of p-NPh from aqueous solutions, as well as a good stability under the chosen experimental conditions.

CHAPTER III

THEORY

The NO_x trapping materials can be found among the alkali and alkaline earth metal oxides, where BaO has been most extensively studied experimentally [33]. Co and Pb mixed oxides developed in our laboratory were effectively used as soot oxidation catalysts in the previous tests [34] and on-board experiments [35] conducted in TOFAŞ. It is investigated if they can also be used as NO_x storage and/or reduction catalysts. For this purpose, first of all thermodynamic calculations were done for the desired catalysts CoO and PbO in order to compare the conversions with BaO for different temperatures.

The storage reactions by using BaO, CoO and PbO respectively are given below:



Thermodynamic tables were used for the equilibrium calculations. Thermodynamic properties of the components at oxidation states of (+2) are given in Table 3.1. All oxidation states, physical and thermodynamic properties of these compounds are given in Appendix A

Table 3.1 Thermodynamic Properties of the Components [36,37]

	$\Delta H^\circ(\text{kJ/mol})$	$\Delta G^\circ (\text{kJ/mol})$	$S^\circ (\text{J/mol K})$	$C_p (\text{J/molK})$
BaO	-558.0	-528.0	70.3	47.4
CoO	-239.0	-213.0	43.9	55.2
PbO	-218.0	-188.0	69.4	49.0
Ba(NO ₃) ₂	-992.0	-795.0	214.0	151.4
Co(NO ₃) ₂	-420.5			
Pb(NO ₃) ₂	-449.0			
NO ₂	33.9	51.8	240.0	37.9
O ₂	0	0	205.0	29.4

$\Delta H^\circ_{\text{rxn}}$, $\Delta G^\circ_{\text{rxn}}$ and $\Delta S^\circ_{\text{rxn}}$ of the equations were calculated by using the following formula:

$$\Delta H^\circ_{\text{rxn}}(298.15 \text{ K}, 1 \text{ atm}) = \sum_i \nu_i \Delta H^\circ_{f,i}(298.15 \text{ K}, 1 \text{ atm}) \quad (1.4)$$

$$\Delta G^\circ_{\text{rxn}}(298.15 \text{ K}, 1 \text{ atm}) = \sum_i \nu_i \Delta G^\circ_{f,i}(298.15 \text{ K}, 1 \text{ atm}) \quad (1.5)$$

$$\Delta S^\circ_{\text{rxn}}(298.15 \text{ K}, 1 \text{ atm}) = \sum_i \nu_i \Delta S^\circ_{f,i}(298.15 \text{ K}, 1 \text{ atm}) \quad (1.6)$$

Due to the fact that all thermodynamic data were not available in the literature for Co(NO₃)₂ and Pb(NO₃)₂, an assumption was done. Since the chemical structures are similar, $\Delta S^\circ_{\text{rxn}}$ of reaction (1.1) is considered to be equal with reactions (1.2) and (1.3). $\Delta G^\circ_{\text{rxn}}$ of the equations (1.2) and (1.3) were calculated according to the following formula where initial temperature is 298 K.

$$\Delta G = \Delta H - T\Delta S \quad (1.7)$$

After that $\Delta G_{\text{rxn}}^{\circ}$ of the equations were calculated, equilibrium constants were determined by using the formula below:

$$K_a(T) = \exp\left(-\frac{\Delta G_{\text{rxn}}^{\circ}}{RT}\right) \quad (1.8)$$

By using the relation between the equilibrium constant and the specific activities of species, conversions were calculated for different temperatures where NO_x is 1000ppm and O_2 is around 10 percent [38].

$$K_a(T) = \prod_{i=1} a_i^{v_i} \quad (1.9)$$

$$\ln[K_{\text{eq}}(T_2)/K_{\text{eq}}(T_1)] = -(\Delta H_{\text{rxn}}/R)*[(1/T_2)-(1/T_1)] \quad (1.10)$$

The calculated equilibrium conversion comparison of BaO with PbO and CoO catalysts is seen in Fig. 3.1. As it is observed, conversions of PbO and CoO are almost compatible with BaO at low temperatures. It may be concluded that desired Co and Pb metal oxide catalysts are convenient for the future applications of the laboratory studies.

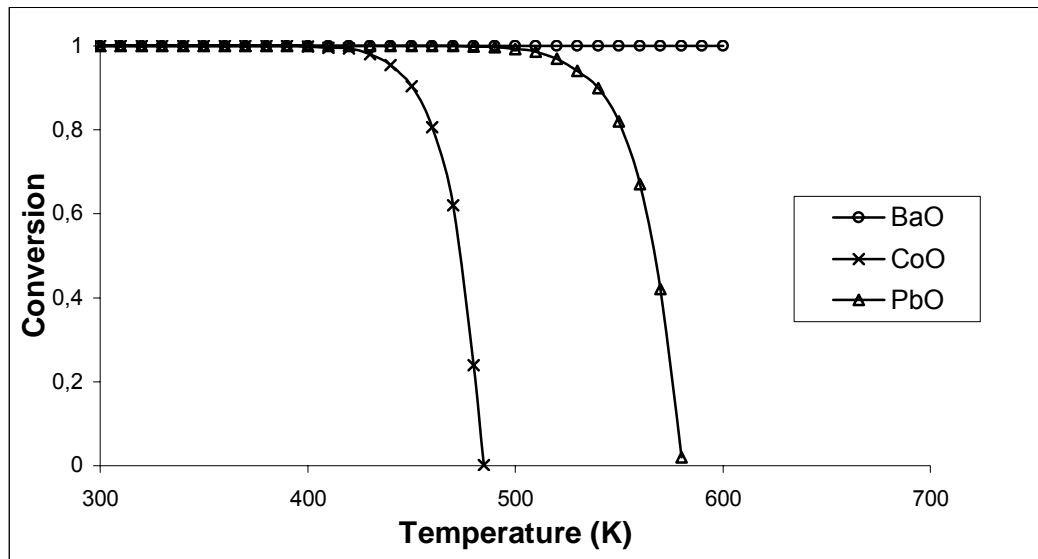


Figure 3.1 Equilibrium Conversion versus Temperature Graph for BaO, CoO and PbO

The detailed equilibrium conversion calculations for each compound (BaO, CoO and PbO) can be seen in Appendix B.

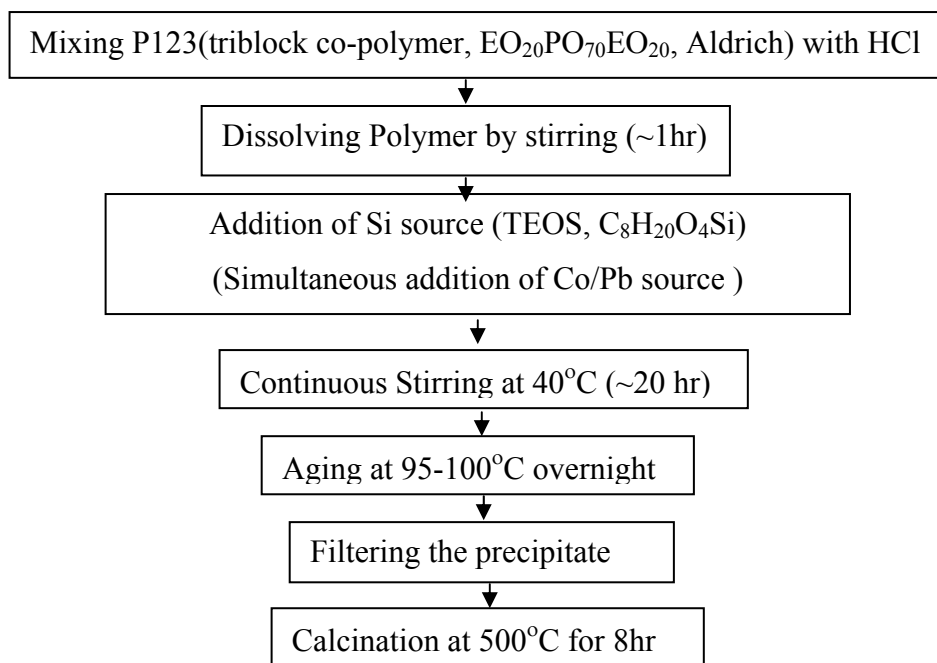
CHAPTER IV

EXPERIMENTAL

4.1 Catalyst Preparation

In this study SBA-15 and Co and/or Pb incorporated mesoporous silica materials were synthesized by Pluronic 123 nonionic triblock co-polymer as template which is a surfactant showing the ability to form liquid-crystal structures. Pluronics are used to synthesize a variety of different ordered mesoporous materials and to obtain high surface area and large pore sizes.

The synthesis of the pure and metal doped SBA-15 mesoporous silica materials were performed by following the procedure below.



4.1.1 Synthesis of Mesoporous SBA-15 Silica

Silica SBA-15 was prepared according to the method reported in the literature [22]. 4 g Pluronic 123 (triblock co-polymer, $\text{EO}_{20}\text{PO}_{70}\text{EO}_{20}$, Aldrich) was dissolved in 150 ml HCl (37%, Riedel-de Haen) (1.6 M) with stirring at room temperature for 1 hour. Afterwards, 8.8 g TEOS ($\text{C}_8\text{H}_{20}\text{O}_4\text{Si}$, Merck) was added to the solution as precursor with stirring at 35-40 °C for 20 hours. The mixture was aged to prevent bulk formation at 95-100°C for 24 hours. The white powder was obtained through filtration. The product was calcined at 500°C for 8 hours.

4.1.2 Synthesis of Co/ SBA-15, Pb/SBA-15 and Co/Pb/SBA-15

4 g Pluronic 123 (triblock co-polymer, $\text{EO}_{20}\text{PO}_{70}\text{EO}_{20}$, Aldrich) was dissolved in 150 ml HCl (1.6 M) with stirring at room temperature for 1 hour. Afterwards, appropriate amount of TEOS was added to the solution considering the weight percentages of added $(\text{CH}_3\text{COO})_2\text{Pb}\cdot 3\text{H}_2\text{O}$ (Merck) as Pb source or $\text{CoCl}_2\cdot 6\text{H}_2\text{O}$ (Riedel-de Haen) as Co source with stirring at 35-40 °C for 20 hours. The mixture was aged at 95-100°C for 24 hours. The powder was obtained through filtration. The product was calcined at 500°C for 8 hours.

Co or Pb incorporated SBA-15 samples with 5-20% Pb and 5-40% Co weight loadings were prepared. Co/Pb doped mixed oxide catalysts were also synthesized at different weight percentages all of which can be seen in Appendix C.

4.2. Catalyst Characterization

4.2.1 X-Ray Diffraction Analysis

XRD patterns were measured on a Rigaku-Miniflex diffractometer using Cu $K\alpha$ -ray radiation ($\lambda=1.5405 \text{ \AA}$) operating at 30 kV and 15mA. XRD patterns were recorded

between $2\theta = 1.0\text{--}3.0^\circ$ with 0.005° intervals, 0.2° data collection velocity in one minute; and $2\theta = 5.0\text{--}75.0^\circ$ with 0.05° intervals, 1° data collection velocity in one minute.

4.2.2 BET Surface Analysis

Surface area of the synthesized catalysts were determined by Brunauer, Emet and Teller (BET) method by N_2 adsorption-desorption measured at 77 K on a micromeritics ASAP 2000 volumetric system. The samples were outgassed for 8 h at 363 K in vacuum prior to the nitrogen adsorption measurements at 77 K.

4.2.3 Thermo Gravimetical Analysis (TGA)

TGA analysis was performed using a Dupont 951 TGA instrument. The measurements were carried out with a heating rate of $10^\circ\text{C}/\text{min}$ under both nitrogen and air flow of $75\text{ cc}/\text{min}$ from 30°C to 600°C .

4.2.4 Differential Scanning Calorimeter Analysis (DSC)

Differential scanning calorimeter measurements were carried out on a Dupont 910S analyzer. The measurements were carried out at a heating rate of $5^\circ\text{C}/\text{min}$ under both nitrogen and air flow of from 30°C to 500°C .

4.2.5 TEM Analysis

The pore geometry of the mesoporous silicas were observed by using transmission electronic micrograph (TEM). In transmission electron microscopes measurements, the specimens were dispersed in ethanol and placed on holey copper grids. Tests were conducted on a Philips EM430 electron microscope operating at 200kV .

4.2.6 AAS Analysis

Lead content in the samples was determined by atomic absorbance analysis using Perkin-Elmer 11013 spectrometer after dissolution of the samples in HCl solution.

4.2.7 XPS Analysis

Surface characterization of catalysts for quantification of surface composition, X-ray Photoelectron Spectroscopy (XPS) was performed. The method reveals which chemical elements are present at the surface. The X-ray photoelectron spectra were obtained using Mg K α ($h\nu=1253.6$ eV) unmonochromatized radiation with SPECS spectrometer. The charging effects were corrected by using the C1s peak, as reference for all samples at a binding energy BE of 284.6 eV.

CHAPTER V

RESULTS & DISCUSSION

5.1 X-ray Diffraction Analysis

The XRD measurements were performed in order to gain information about the porous structure and the possible presence of crystalline phases simultaneously.

The XRD patterns of pure SBA-15 and Pb/SBA-15, consisting of different loadings of Pb samples, are given in Fig. 5.1. In the wide angle region XRD pattern ($2\theta = 5-75^\circ$), no characteristic peaks of metal oxide was observed between 5-15 wt% Pb loading in SBA-15 sample, indicating that Pb finely dispersed on the surface of the sample or incorporated in the pore walls of the sample. However, more appreciable characteristic peaks are observed for the sample of 20 wt% Pb loading in SBA-15, indicating small quantities of crystallites of lead oxide existing on the surface of silica. The peaks observed between $2\theta = 20-25^\circ$ were attributed to the presence of SiO_2 , while $2\theta = 30-45^\circ$ demonstrates that lead exists in the form of PbO . The intensities and d values of the compounds with their card numbers are given in Appendix D.

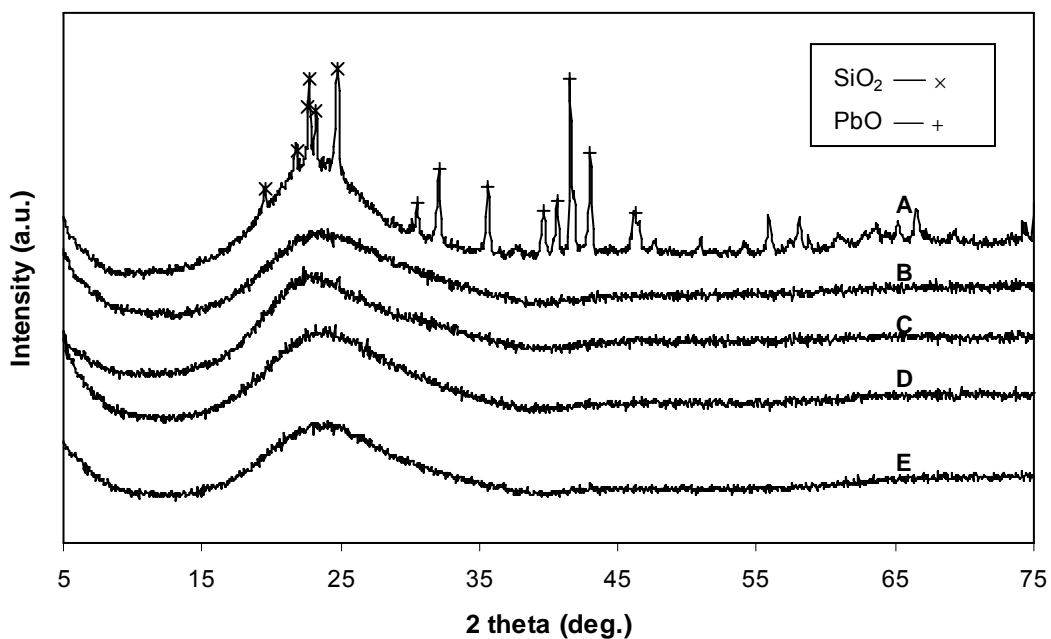


Figure 5.1 Wide angle XRD patterns of Pb/SBA-15 (A) 20%Pb 55%Si, (B) 15%Pb 55%Si, (C) 10%Pb 55%Si, (D) 5%Pb 55%Si, (E) SBA-15

The ordered hexagonal structure of SBA-15 is confirmed by typical diffractions in all Pb loadings as it can be seen in Fig. 5.2. Two characteristic peaks of SBA-15 ($2\theta=1.6, 1.8^\circ$) structure were observed in the low-angle X-ray patterns. For all samples the ordered hexagonal structure of SBA-15 was confirmed by typical reflections at 1.6° and 1.8° from 110 and 200 planes respectively in all Pb loadings. The strong peak at 2θ around 0.8° could not be observed due to the instrumental limitation. Higher intensity of peaks in the XRD pattern of pure SBA-15 than loaded samples shows the decrease in the long-range order of pores by the addition metal oxides. The characteristic peaks shift to higher $2\theta=1.8, 2.1$, which can be seen in Table 5.1, as the Pb loading is increased indicating the decrease in the d spacing. This is probably due to the shrinkage of the surfactant micelles arising from the weakening in the interaction between the silica and surfactant in the high addition of metal oxide during the hydrothermal process.

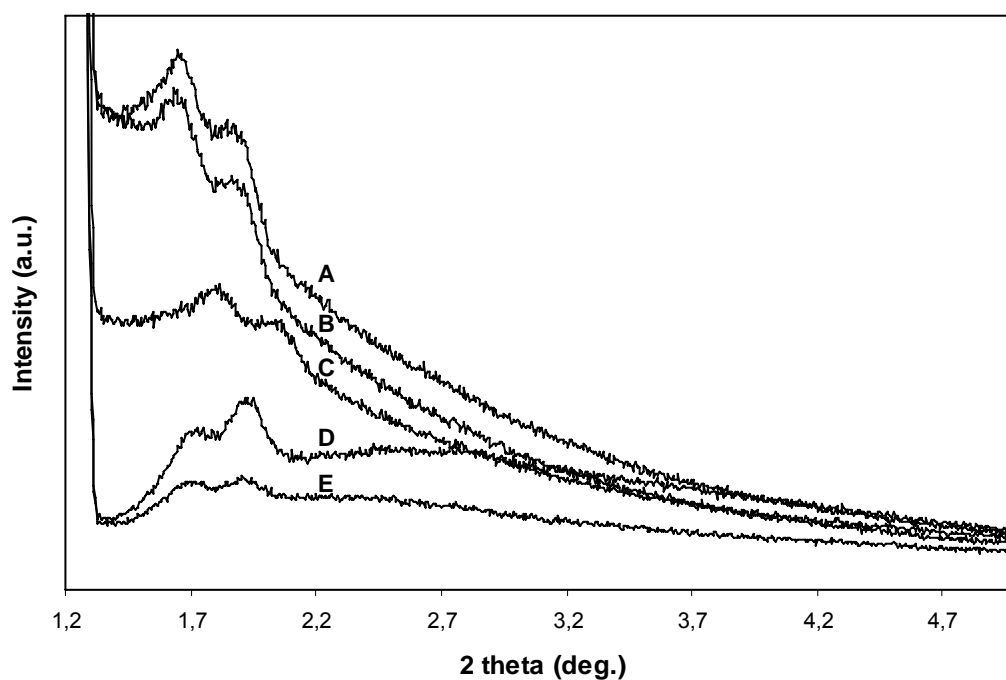


Figure 5.2 Low-angle XRD patterns of Pb/SBA-15 (A) 5%Pb 55%Si, (B) 15%Pb 55%Si, (C) 20%Pb 55%Si, (D) SBA-15, (E) 10%Pb 55%Si

Table 5.1 2θ angles for the peaks of Pb loaded SBA-15

Observed Position of the Peak (2θ)	% Pb loaded SBA-15
1.6/1.8	-
1.6/1.8	5
1.7/1.9	10
1.7/1.9	15
1.8/2.1	20

The presence of intense characteristic peaks of Co in the wide angle XRD signifies the formation of crystallites as it can be seen in Fig. 5.3. In contrast to the lead loading the addition of Co results in crystallization even at 10% loading which

indicates that lead behaves closer to the SBA-15 structure than cobalt. Besides, it indicates that lead is much more dispersed on the surface of the sample when compared with the incorporation of cobalt into SBA-15. The peaks observed at $2\theta \approx 37^\circ$ demonstrates that cobalt exists in the form of Co_3O_4 according to the card number 78-1969 which can be seen in Appendix D.

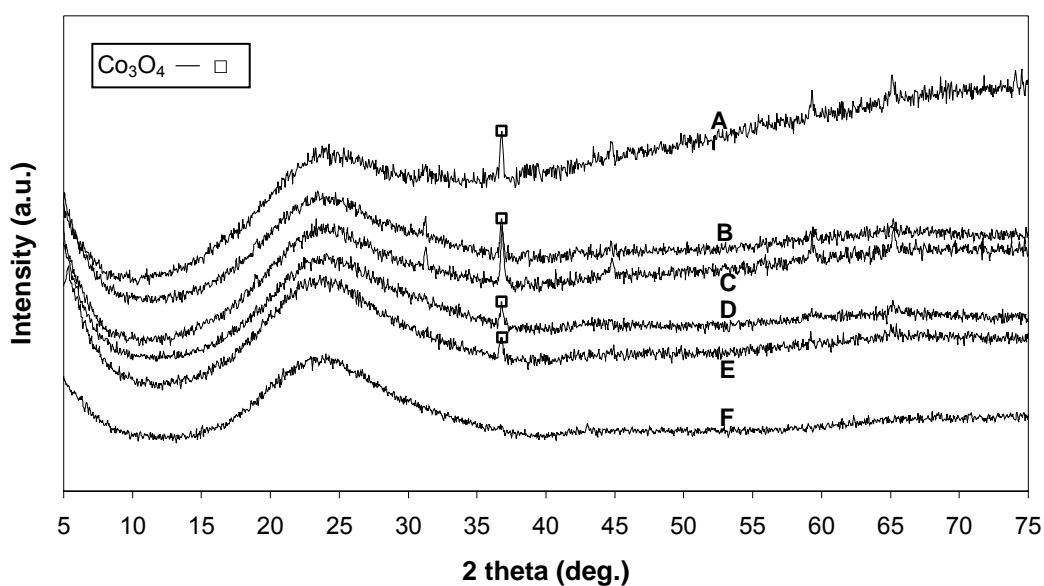


Figure 5.3 Wide angle XRD patterns of Co/SBA-15 (A) 40%Co 40%Si, (B) 20%Co 40%Si, (C) 15%Co 40%Si, (D) 10%Co 40%Si, (E) 5%Co 40%Si, (F) SBA-15

As it can be seen in Fig. 5.4, when the samples are loaded 5-15 %wt Co, the characteristic peaks shift to smaller $2\theta=1.5, 1.7$ which can be seen in Table 5.2, indicating an increase in d-spacing, possibly due to swelling of the surfactant micelles arising from the strong interaction between the metal oxide and surfactant during the hydrothermal process. It can be concluded that cobalt gets incorporated inside the framework and thereby enlarges its pore size.

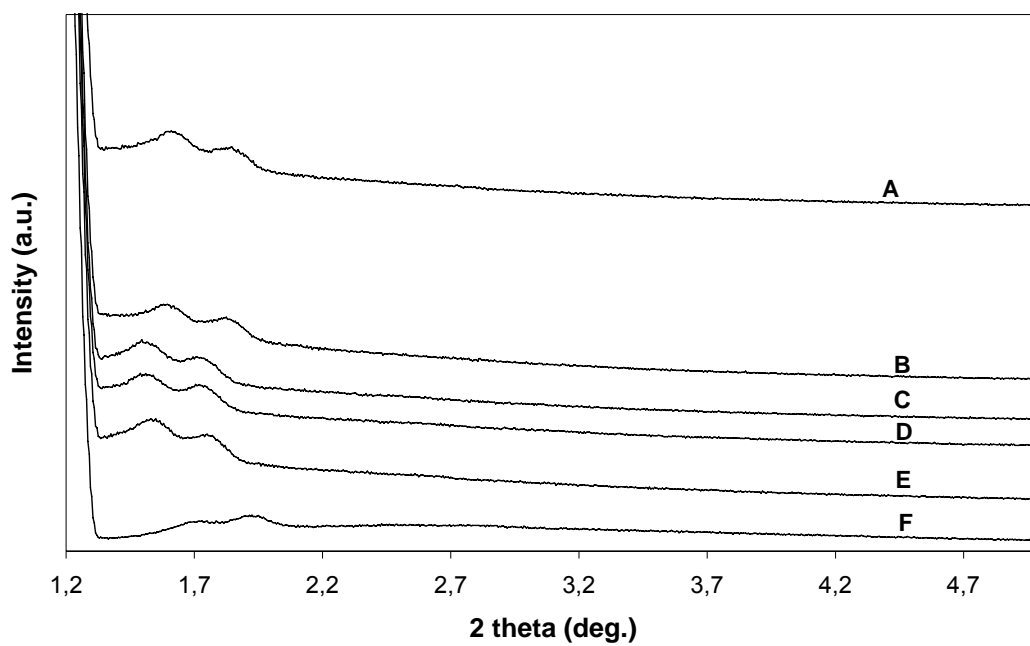


Figure 5.4 Low angle XRD patterns of Co/SBA-15 (A) 40%Co 40%Si, (B) 20%Co 40%Si, (C) 15%Co 40%Si, (D) 10%Co 40%Si, (E) 5%Co 40%Co, (F) SBA-15

Table 5.2 2θ angles for the peaks of Co loaded SBA-15

Observed Position of the Peak (2θ)	% Co loaded SBA-15
1.6/1.8	-
1.5/1.7	5
1.5/1.7	10
1.5/1.7	15
1.6/1.8	20
1.6/1.8	40

As shown in Fig. 5.5, the XRD patterns at high diffraction angles were obtained by incorporating different weight percentages of Pb and Co into SBA-15. The presence of highly intense characteristic peaks of Co and Pb in the pattern indicates that the formation of crystallites increased by the addition of smaller amount of cobalt chloride than lead acetate to the silica. The peaks observed at $2\theta \approx 20-25^\circ$ were attributed to the presence of SiO_2 , while $2\theta \approx 30-35^\circ$ shows the PbO metal oxide structure. The characteristic peak of Co_3O_4 shifts to higher 2θ angle of 40° which may be probably due to the effect of other doped metal oxide (PbO) in the new formed mixed oxide structure.

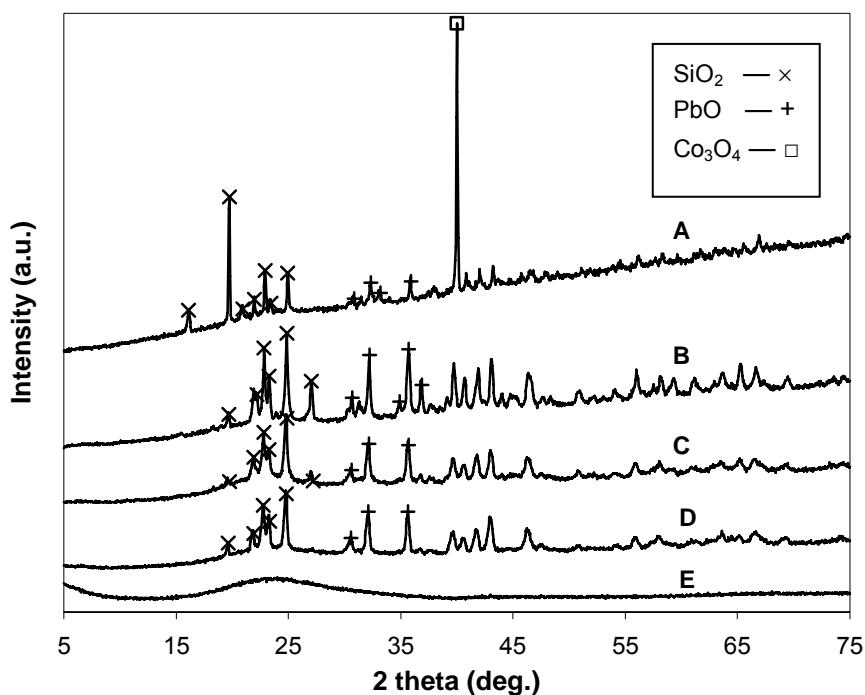


Figure 5.5 Wide angle XRD patterns of Co-Pb/SBA-15 (A) 17%Pb 40%Co 15%Si, (B) 17%Pb 20%Co 15%Si (C) 25%Pb 10%Co 40%Si, (D) 30%Pb 10%Co 40%Si, (E) SBA-15

The long range order was lost in the high amount of metal loading to SBA-15 which is observed in Fig. 5.6, the low angle powder XRD pattern of SBA-15 loaded with cobalt and lead oxides. It can be concluded that there are chemical interactions between host SBA-15 and the guest metal oxides and the strength of these interactions are changing by the type and the amount of metal oxides loaded to samples.

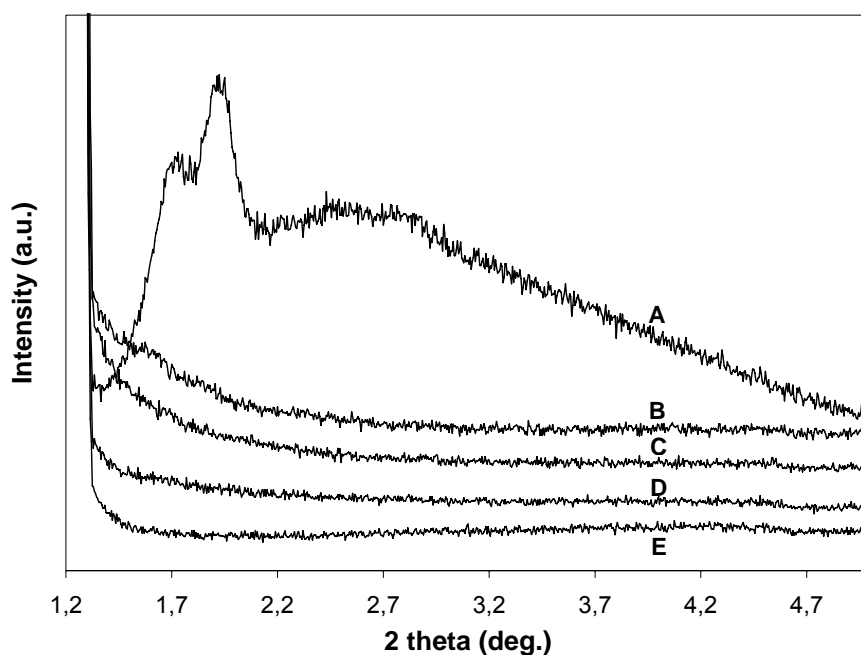


Figure 5.6. Low-angle XRD patterns of Co-Pb/SBA-15 (A) SBA-15, (B) 17%Pb 40%Co 15%Si, (C) 17%Pb 20%Co 15%Si, (D) 25%Pb 10%Co 40%Si, (E) 30%Pb 10%Co 40%Si

5.2 BET Surface Area Measurements

Surface areas were calculated by BET (Brunauer-Emmett-Teller) method and pore size distributions were determined using the BJH (Barrett-Joyner-Halenda) method.

Fig. 5.7 shows nitrogen adsorption/desorption isotherms for siliceous SBA-15, Co/SBA-15, Pb/SBA-15 samples. All of the nitrogen adsorption/desorption isotherms are the type of IV in nature according to the IUPAC classification and exhibited an H1 hysteresis loop which is a characteristic of mesoporous solids.

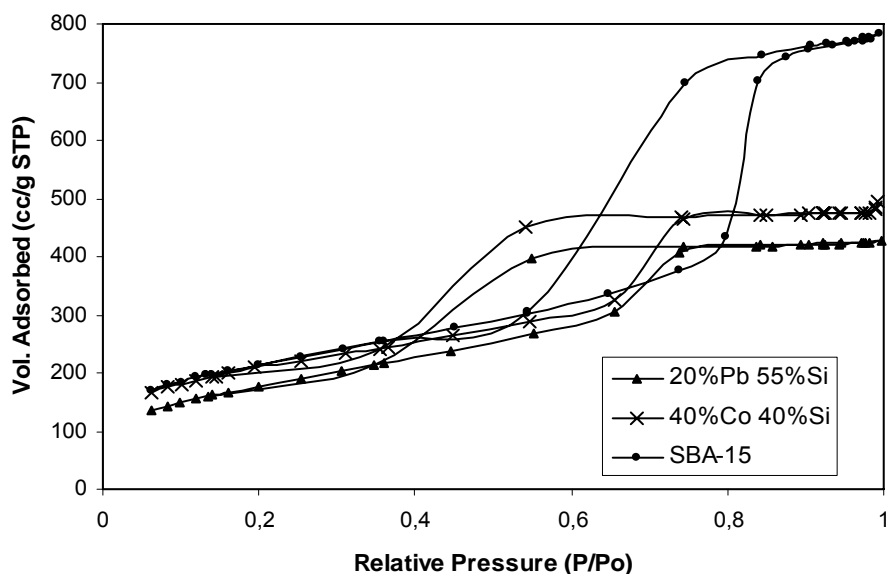


Figure 5.7. Nitrogen adsorption-desorption isotherms for the mesoporous silicas

The increase in the loadings of metals in SBA-15 causes a decrease in the surface area due to the substitution of pores with metal atoms (Table 5.3). The decrease in surface area may be due to the partial blockage of pores by forming cobalt oxide particles inside the pore channels. The decrease in the pore volume by metal loading is in agreement with the surface area measurements.

The estimated textural parameters such BET surface area, adsorption average pore diameter, and cumulative adsorption pore volumes for various samples are shown in Table 5.3.

Table 5.3 The mixed oxide catalyst compositions and surface areas

Sample	Si wt %	Co wt%	Pb wt%	O ₂ wt %	BET surface area (m ² /g)	D _{BJH} (Å°)	V _{BJH} (cm ³ /g)
SBA-15	56	-	-	44	772.5	71.2	1.2
Co/SBA-15	40	5	-	55	562.1	51.4	0.8
	40	10	-	50	409.1	47.9	0.6
	40	15	-	45	474.9	48.4	0.7
	40	20	-	40	475.3	46.3	0.7
	40	40	-	20	747.5	46.8	0.7
Pb/SBA-15	55	-	5	40	551.3	41.9	0.7
	55	-	10	35	353.6	77.3	0.8
	55	-	15	30	501.7	42.4	0.6
	55	-	20	25	648.9	44.3	0.7
Co-Pb/SBA-15	15	40	17	28	57.7	376.5	0.6
	15	20	17	48	25.8	129.9	0.1
	40	10	25	25	58.6	78.7	0.1
	40	10	30	20	207.7	67.2	0.4

5.3 Thermal Analysis by TGA/DSC

TGA and DSC analyses were performed in order to determine whether the calcination temperatures for the samples are convenient and for the observation of phase transitions respectively. Weight loss under inert medium which was observed in TGA plots was attributed to the desorption of volatile fraction (H₂O, HCs, etc.). DSC plots showed the presence of heat flows and phase transformations at several

temperatures. Endothermic peaks were more obvious for Co and Pb loaded sample which shows endotherms at several temperatures probably due to the melting of lead clusters that exist in metallic form. TGA/DSC plots of Co and/or Pb loaded SBA-15 samples are given in Appendix E.

5.4 TEM Analysis

The TEM image of pure SBA-15 which can be seen in Fig. 5.8 confirms the ordered structure of the material, and shows the cylindrical pores are arranged in an ordered hexagonal array.

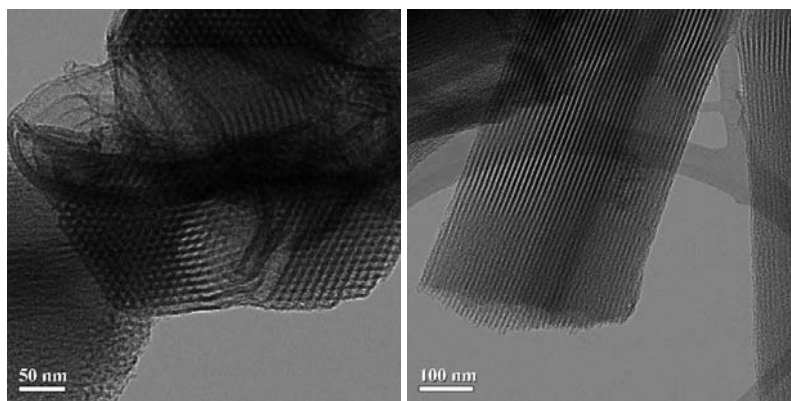


Figure 5.8 TEM images of pure SBA-15

As it can be seen in Fig. 5.9, 5 %wt Pb loaded SBA-15 shows partially ordered structure and majority of the sample is nonstructured. The catalysts possess the typical two-dimensional hexagonal structure of SBA-15.

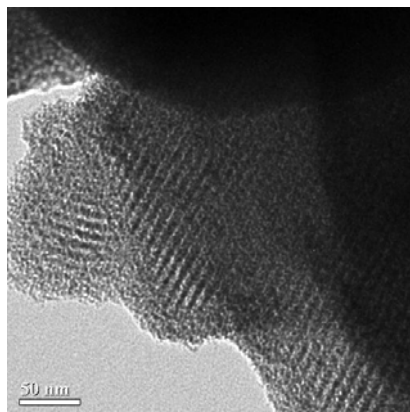


Figure 5.9 TEM image of 5%Pb 55%Si

20 wt% Pb loaded sample shows a novel onion-type structure as it is given in Fig. 5.10. It has an amorphous silicate core and hexagonal mesostructured shell.

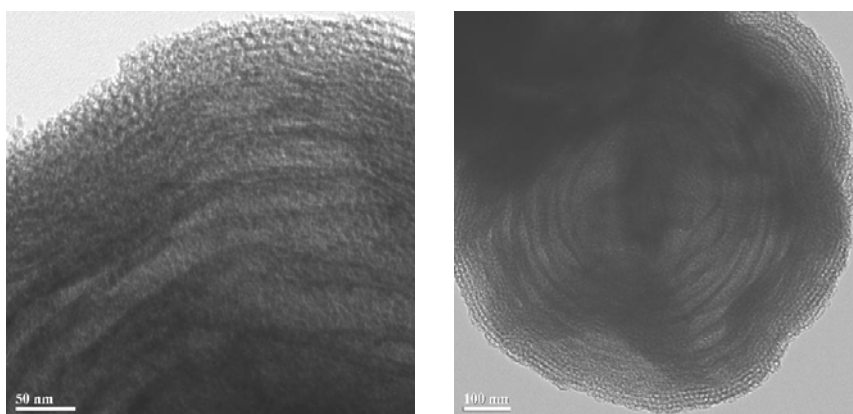


Figure 5.10 TEM images of 20%Pb 55%Si

In Co loaded samples into SBA-15 which can be seen in Figures 5.11 and 5.12, show highly ordered mesostructures. No nanoparticles were found within the mesochannels. TEM images show the characteristic wormhole-like morphology for both the cobalt-containing samples. Cobalt-grafted samples also show the presence

of agglomerated particles. The samples also possess the typical two-dimensional hexagonal structure of SBA-15.

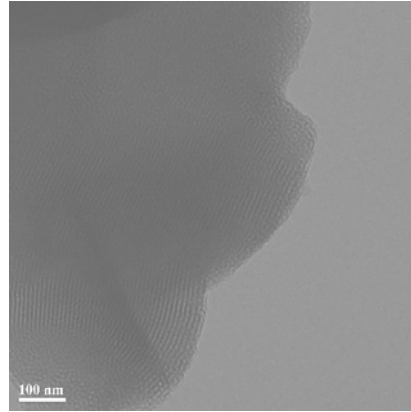


Figure 5.11 TEM image of 10%Co 40%Si

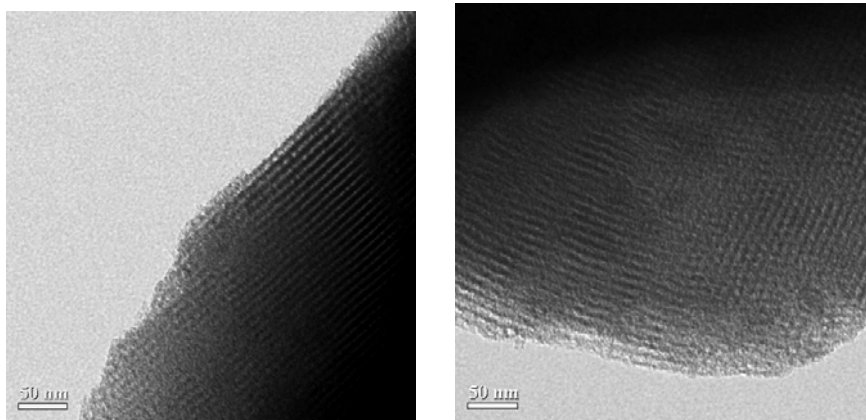
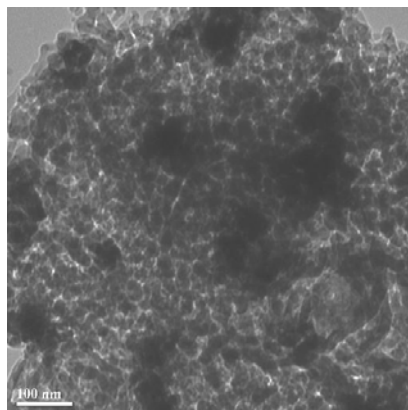


Figure 5.12 TEM images of 40%Co 40%Si

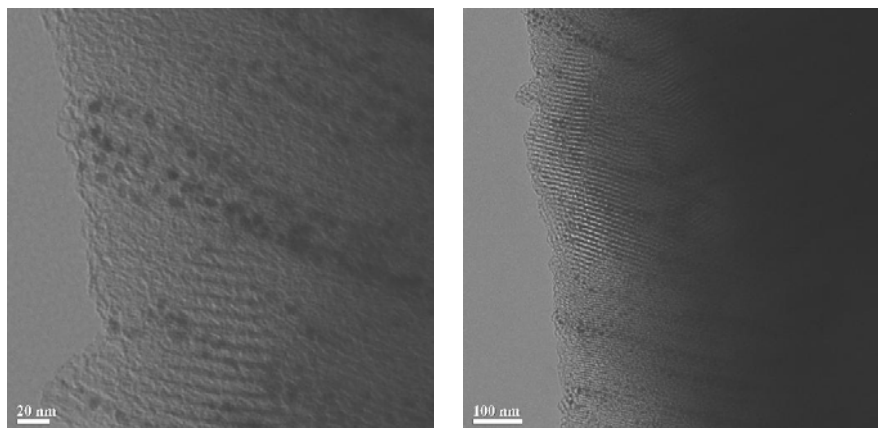
The size of the nanoparticles are at ~ 20 nm in the 17%Pb 40%Co 15%Si sample as it can be seen in Fig. 5.13.



5.13 TEM image of 17%Pb 40%Co 15%Si

In the 10%Co 25%Pb 40%Si sample, nanoparticles are well and periodically located within mesochannels of SBA-15 materials, like pearl necklace as it is given in Fig.

5.14. Some large nanoparticles are also observed in the structure.



5.14 TEM images of 10%Co 25%Pb 40%Si

5.5. Quantitative Analysis by AAS

By using atomic absorbance analysis, it is investigated if there exists lead in the samples after the calcination at high temperatures. It is observed that lead still exists in the samples in spite of the high calcination temperatures as seen in Table 5.4.

Table 5.4. Lead Content of the Samples

Sample	Intended wt Pb% loading	Actual wt Pb% loading
5%Pb 55%Si	5	0.9
10%Pb 55%Si	10	4.1
15%Pb 55%Si	15	1.3
17%Pb 20%Co 15%Si	17	13.9
17%Pb 40%Co 15%Si	17	15.1
25%Pb 10%Co 40%Si	25	12.5
30%Pb 10%Co 40%Si	30	9.6

5.6 XPS Analysis

Surface characterization of Pb and Co was performed by XPS for revealing the oxidation states of the species. From XPS data, signals detected that binding energies of 136.6 eV for Pb 4f_{7/2} and 530.5 for eV for O1s indicated the presence of PbO oxide layer in the 20%Pb loaded SBA-15 which can be seen in Fig. 5.15. The B.E. value of 4f core level for Pb loaded sample exhibiting 136.6 eV is in accordance with most of the literature data [39].

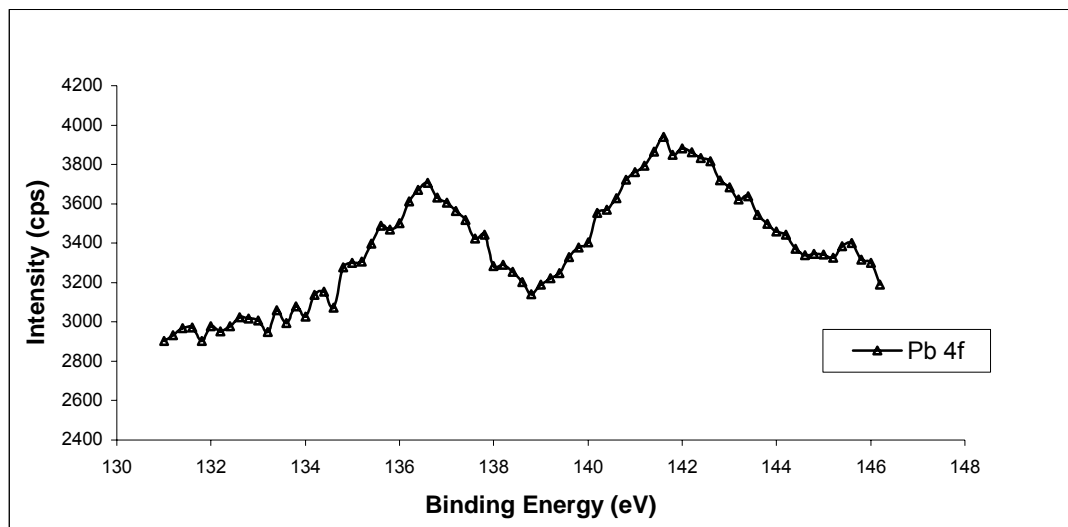


Figure 5.15 XPS Spectra of Pb 4f levels for 20%Pb 55%Si catalyst

As it is seen in Fig. 5.16, binding energies of 782.6 eV for Co $2p_{3/2}$ and 531 for eV for O1s indicated the presence of CoO or Co_3O_4 in the 40%Co loaded SBA-15 since the cobalt oxides CoO and Co_3O_4 might show similar XPS spectra [40]. 531 eV for O1s is coming from oxygen bonded in compound with Co. Such a low value of oxygen B.E. on Co_3O_4 indicates higher mobility and reactivity of oxygen. Cobalt oxide (Co_3O_4) exhibits two oxidation states. On a molar basis, there are two Co^{3+} in octahedral symmetry and one Co^{2+} in tetrahedral symmetry. A range of values has been reported for the binding energies of Co^{2+} and Co^{3+} ; a part of the range is due to the reference used. For example, Sexton et al. reported a binding energy of 780.3 eV for Co^{2+} and 779.5 eV for Co^{3+} ; the binding energy of the higher valence state usually has the higher binding energy [41 and references therein].

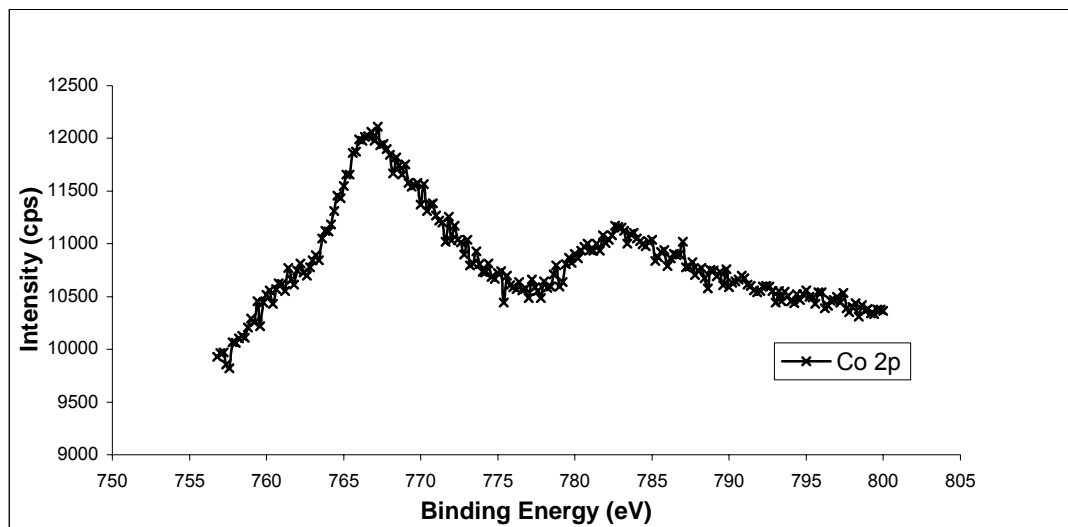


Figure 5.16 XPS Spectra of Co 2p levels for 40%Co 40%Si catalyst

XPS data obtained for Pb or Co loaded SBA-15 and Pb-Co loaded SBA-15 samples exhibiting the Pb 4f and Co 2p levels are seen in Figures 5.17 and 5.18 respectively. A shift occurs to higher binding energies for Pb-Co loaded samples when compared with pure Pb or Co loaded samples which can be seen in Table 5.5. This is most likely due to the $\text{Co}_3\text{O}_4 \rightarrow \text{CoO}$ transition, as Co^{3+} ions in the spinel structure at the lower binding energy are reduced to a +2 valence state at higher binding energy [41].

Table 5.5 Binding Energies of Co 2p and Pb 4f levels for Pb or Co and Pb-Co loaded SBA-15 samples

Sample	BE of Co 2p (eV)	BE of Pb 4f (eV)
40%Co 40%Si	782.6	-
20%Pb 55%Si	-	136.6
17%Pb 20%Co 15%Si	784.8	139.3
17%Pb 40%Co 15%Si	784.8	139.3
25%Pb 10%Co 40%Si	784.2	140.6
30%Pb 10%Co 40%Si	785.2	139.1

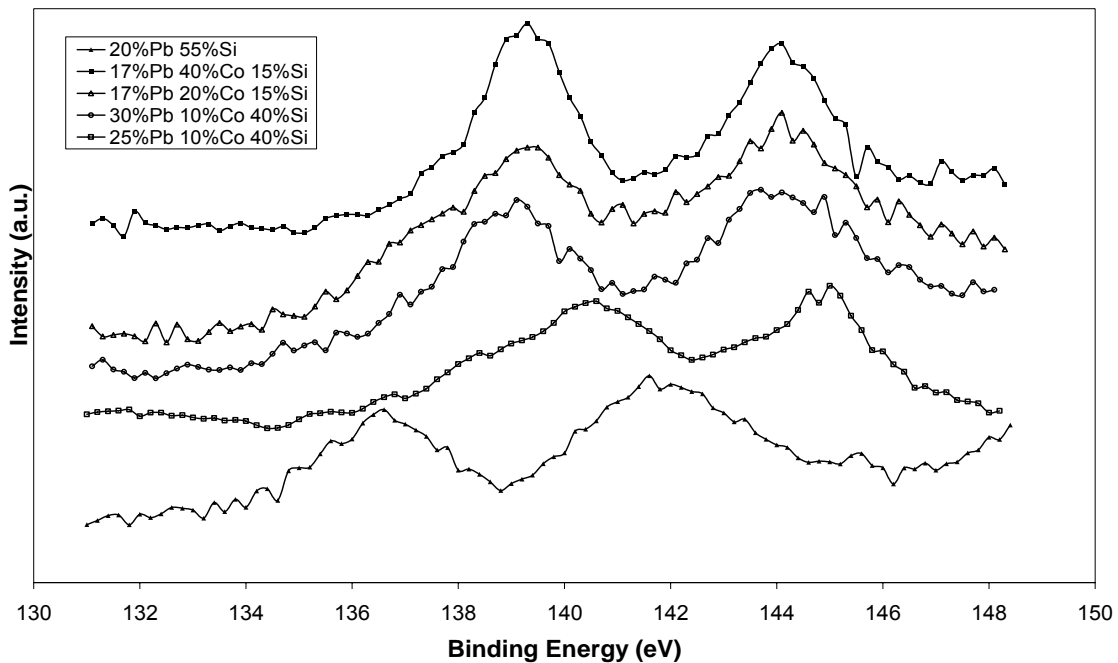


Figure 5.17 XPS Spectra of Pb 4f levels for Pb/SBA-15 and Co-Pb/SBA-15 samples

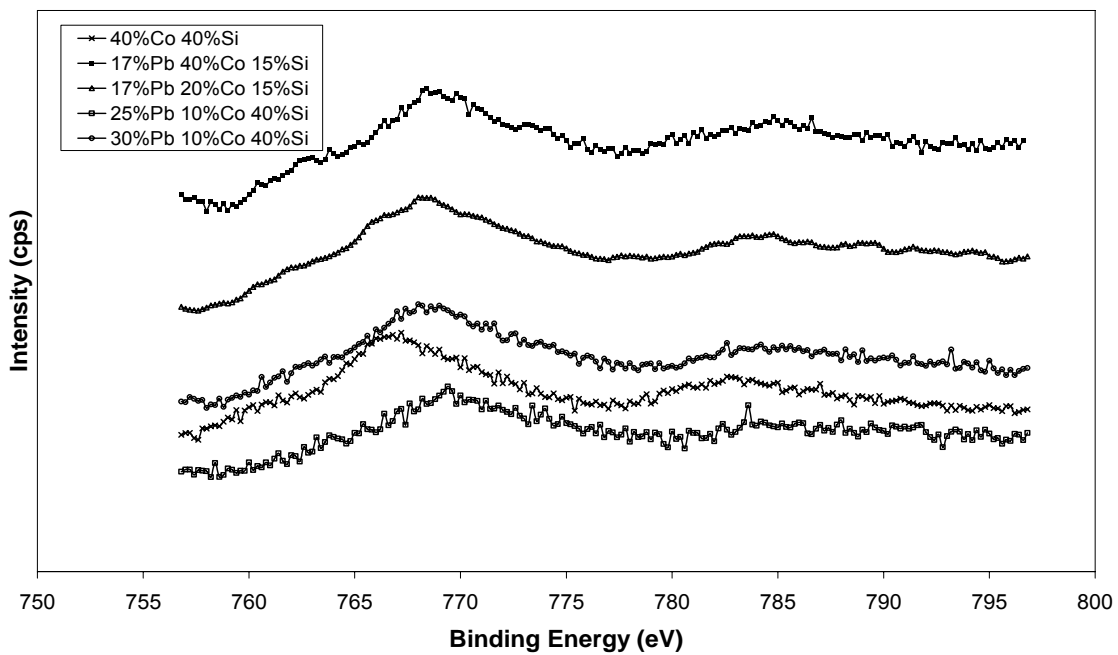


Figure 5.18 XPS Spectra of Co 2p levels for Co/SBA-15 and Co-Pb/SBA-15 samples

The binding energies of O, for Pb or Co loaded SBA-15 was nearly similar at values of 530.7 and 531 eV respectively. However, a shift occurs to a higher binding energy of nearly 533 eV for Co and Pb loaded samples as it can be seen in Fig. 5.19.

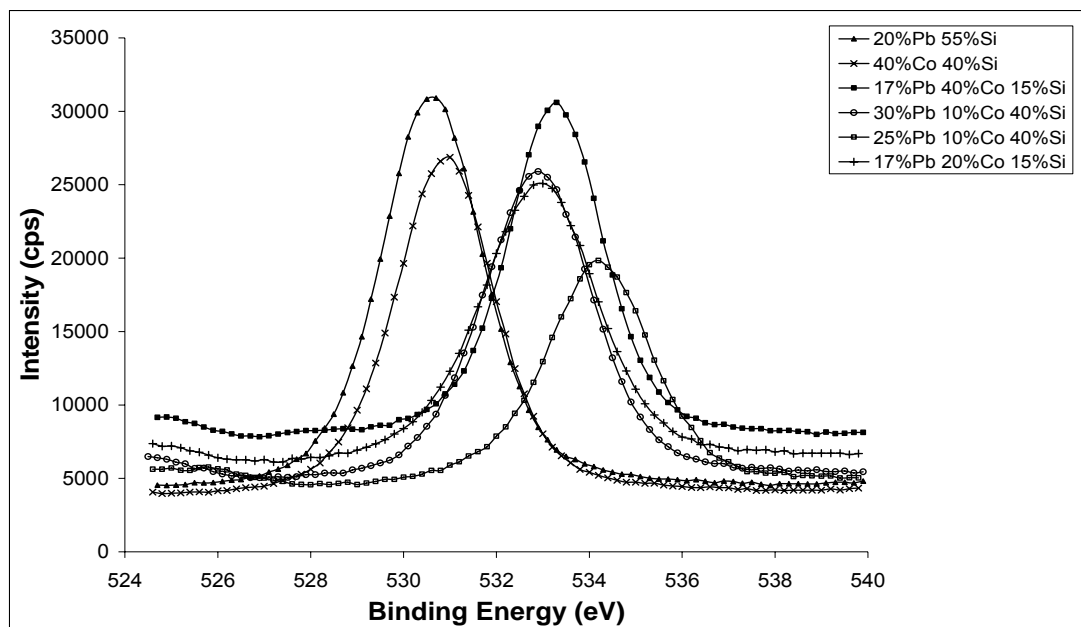


Figure 5.19 XPS profiles of O 1s for different metal loaded catalysts

A similar trend was observed for Si in Fig. 5.20. The binding energies of Si for Co or Pb loaded SBA-15 samples are at values of 101.5 and 101.4 eV respectively, while BE of Si for the mixed oxide loaded samples is nearly at 103.7 eV. The binding energies for O 1s and Si 2p for the metal oxide loaded samples are seen in Table 5.6.

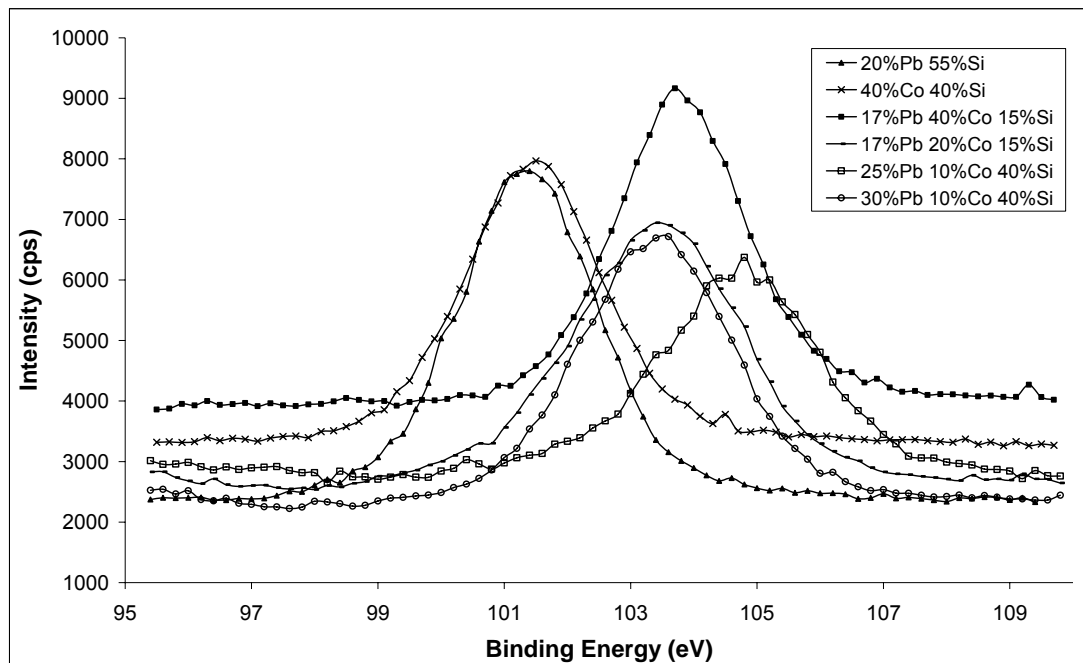


Figure 5.20 XPS profiles of Si 2p for different metal loaded catalysts

Table 5.6 Binding Energies of O 1s and Si 2p levels for Pb or Co and Pb-Co loaded SBA-15 samples

Sample	BE of O 1s (eV)	BE of Si 2p (eV)
20%Pb 55%Si	530.5	101.4
40%Co 40%Si	531	101.5
17%Pb 20%Co 15%Si	533	103.4
17%Pb 40%Co 15%Si	533.1	103.7
25%Pb 10%Co 40%Si	534.2	104.8
30%Pb 10%Co 40%Si	532.9	103.6

CHAPTER VI

CONCLUSION

Co and Pb incorporated SBA-15 mesoporous materials were synthesized by direct synthesis method by using cobalt chloride as cobalt source and lead acetate as lead source. By loading 5, 10, 15 wt % Pb into SBA-15, any characteristic peak of metal oxide crystal can not be observed in the large angle XRD pattern ($2\theta=5-75^\circ$). Similar results were obtained for cobalt loaded samples up to 10 wt% loading. Thus, it is concluded that metal particles are dispersed in the SiO_2 structure without accumulating and forming a crystal in a certain part of the framework. Incorporation of 20 wt% Pb into SBA-15 indicated more appreciable characteristic peaks which leads to the formation of crystallites over the structure. In contrast to the Pb loading, the addition of Co results in crystallization even at 10% loading. This can be explained that small quantity of crystallites of metal oxide exists on the surface of silica. The hexagonal structure of SBA-15 was observed for all samples via the small angle XRD pattern consisting of two weak peaks at 2θ around 1.6 and 1.8°. Higher intensity of peaks of pure SBA-15 than loaded samples in the XRD pattern indicates the decrease in the long-range order of pores by the addition metal oxides. The incorporation of high amount of cobalt and lead oxides to SBA-15 as metal oxides leads the long range order to disappear. It can be concluded that there are chemical interactions between host SBA-15 and the guest metal oxides.

By BET analysis, a decrease in the surface areas was observed by increasing the loadings of metals in SBA-15 which may be due to the filling of pores with metal atoms. All of the nitrogen adsorption/desorption isotherms showed type IV hysteresis loop which indicates the mesoporous structure.

The TEM images of the Pb and Co loaded samples indicate that the catalysts possess the typical two-dimensional hexagonal structure of SBA-15. Larger nanoparticles were observed in the Co and Pb mixed oxide catalysts. The TEM results showed that the cobalt and lead oxides are highly dispersed in the silicon framework.

Binding energies of O₂ and Si are nearly similar in Co or Pb incorporated SBA-15 sample according to the XPS analysis. However, Co-Pb/SBA-15 mixed oxide sample showed higher binding energies which may lead to a different growth structure.

High surface areas and controlled geometries in nanometer scale were obtained in the carried out laboratory experiments which make them useful in partial oxidation and NO_x storage and reduction catalysis.

REFERENCES

[1] Diesel and Gasoline Engines

<http://www.howstuffworks.com/diesel.htm>

(last accessed 20th September, 2006)

[2] Kašpar, J., Fornasiero, P., Hicke N., Catalysis Today **77**, 419–449 (2003)

[3] Exhaust Emission Pollutants

<http://www.epa.gov/ord/NRMRL/pubs/chap2.pdf>

(last accessed 20th September, 2006)

[4] Gill, L. J., Blakeman, P. G., Twigg, M. V., Walker, A. P., Topics in Catalysis **28**, 1–4 (2004)

[5] Neft, J., Makkee, M., Moulijn, J., Fuel Processing Technology **47**, 1-69 (1996)

[6] Siegmann, K., Scherrer, L., Siegmann, H.C., Journal of Molecular Structure **458**, 191 (1998)

[7] Diesel Emissions and Diesel-Emission Control Technologies

<http://www.engelhard.com/documents/FAQ-Diesel-ptx.pdf>

(last accessed 20th September, 2006)

[8] Emission Standards

<http://www.dieselnet.com/standards/eu/hd.php>

(last accessed 20th September, 2006)

[9] Fritz, A., Pitchon, V., Applied Catalysis B: Environmental **13**, 1-25 (1997)

[10] Misonoa, M., Inuibe, T., Catalysis Today **51**, 369-375 (1999)

[11] Fridell, E., Skoglundh, M., Westerberg B., Johansson, S., Smedler, G., Journal of Catalysis **183**, 196–209 (1999)

- [12] Komatsu, T., Tomokuni, K., Yamada, I., *Catalysis Today* **116**, 244–249 (2006)
- [13] Xia, Y. and Mokaya, R., *J. Mater. Chem.* **13**, 3112–3121 (2003)
- [14] Lu, Q., Gao, F., Komamemi, S., Mallouk, T. E., *J. Am. Chem. Soc.* **126**, 8650–8651 (2004)
- [15] Xiao, F. S., *Topics in Catalysis Vol.* **35**, 1–2 (2005)
- [16] Walcarius, A., *C. R. Chimie* **8**, 693–712 (2005)
- [17] Kónya, Z., Zhu, J., Szegedi, A., Kiricsi, I., Alivisatos, P., Somorjai, G. A., *Chem. Commun.*, 314–315 (2003)
- [18] Taguchi, A., Schüth, F., *Microporous and Mesoporous Materials* **77**, 1–45 (2005)
- [19] On, D. T., Giscardi, D. D., Danumah, C., Kaliaguine, S., *Applied Catalysis A: General* **222**, 299–357 (2001)
- [20] Jana, S. K., Nishida, R., Shindo, K., Kugita, T., Namba, S., *Microporous and Mesoporous Materials* **68**, 133–142 (2004)
- [21] Campbell, R.; Bakker, M.; Treiner, C.; Chevalet, J., *J. Porous Mater.* **11**, 63–69 (2004)
- [22] Zhao, D., Huo, Q., Feng, J., Chmelka, B. F., Stucky, G. D., *J. Am. Chem. Soc.* **120**, 6024–6036 (1998)
- [23] Ciesla, U., Schüth, F., *Microporous and Mesoporous Materials* **27**, 131–149 (1999)
- [24] Vra°lsted, T., Øye, G., Sjöblom, J., Stöcker, M., *Journal of Dispersion Science and Technology* **27**, 489–496 (2006)
- [25] Tuel, A., *Microporous and Mesoporous Materials* **27**, 151–169 (1999)
- [26] Perego, C., Villa, P., *Catalysis Today* **34**, 281–305 (1997)
- [27] Wang, Y., Wang, X., Su, Z., Guo, Q., Tang, Q., Zhang, Q., Wan, H., *Catalysis Today* **93–95**, 155–161 (2004)
- [28] Xi, J., Tang, X., *Electrochimica Acta* **50**, 5293–5304 (2005)
- [29] Cattarin, S., Guerriero, P., Musiani, M., *Electrochimica Acta* **46**, 4229–4234 (2001)

- [30] Casellato, U., Cattarin, S., Musiani M. b, *Electrochimica Acta* **48**, 3991-3998 (2003)
- [31] Petrova, M., Stefanov, Y., Noncheva, Z., Dobrev, T., Rashkov, S., *British Corrosion Journal* **34**, No:3 (1999)
- [32] Quiroz, M.A., Reyna, S., Marti´nez-Huitle, C.A., Ferro, S., De Battisti, A., *Applied Catalysis B: Environmental* **59**, 259-266 (2005)
- [33] Broqvist, P., Grönbeck, H., Fridell, E., Panas, I, *Catalysis Today* **96**, 71–78 (2004)
- [34] Uner, D., Demirkol, M.K., Dernaika, B., *Applied Catalysis B: Environmental* **61**, 359-370 (2005).
- [35] Genc, V.E., Altay, F.E., Uner, D., *Catalysis Today* **105**, 537-543 (2005)
- [36] Lide, D.R., *CRC Handbook of Chemistry and Physics*, 73rd Edition, CRC Press, 1993
- [37] Speight, J.G., *Perry’s Standard Tables and Formulas for Chemical Engineers*, Mc Graw Hill, 2003
- [38] Monticelli, O., Loenders, R., Jacobs, P. A., Martens, J. A., *Applied Catalysis B: Environmental* **21**, 215–220 (1999)
- [39] XPS Database
<http://www.lasurface.com/database/elementsxps.php>
(last accessed 20th September, 2006)
- [40] Liao, C.L., Lee, Y.H., Chang, S.T., Fung, K.Z., *Journal of Power Sources*, Article in Press (2005)
- [41] Jacobs, G., Chaney, J. A., Patterson, P. M., Dasa, T. K., Davis, B. H., *Applied Catalysis A: General* **264**, 203–212 (2004)
- [42] *Physical Properties of Elements and Compounds*
<http://www.webelements.com>
(last accessed 20th September, 2006)
- [43] Chase, W.C., *NIST-JANAF Thermodynamic Tables*, 4th Edition, 1998

APPENDIX A

PHYSICAL and THERMODYNAMIC PROPERTIES OF Pb and Co OXIDES

Table A1. Physical Properties and Oxidation States of Pb Oxides [42]

	Element	Formal oxidation state	MW(g)	Melting Point (°C)	Color	Density (kg/m ³)
Pb	Pb	0	207.2	327.5	Bluish white	11340
PbO	Pb O	2 -2	223.2	888	Red or yellow	9350
PbO ₂	Pb O	4 -2	239.2	290 (decomposes to Pb ₃ O ₄)	Brown or red	9640
Pb ₂ O ₃	Pb O	3 -2	462.4	530 (decomposes to Pb ₃ O ₄)	Black	10000
Pb ₃ O ₄	Pb O	4 -2	685.6	830	Orange-red	8300

Table A2. Thermodynamic Properties of Pb Oxides [43]

	ΔH_f° at 298.15 K (kJ/mol)	ΔG_f° at 298.15 K (kJ/mol)	S° (J/mol K)	C_p (J/mol K)
Pb(s)	0	0	64.81	26.44
Pb(g)	195.0	161.9	175.373	20.786
PbO(s) yellow	-218.062	-188.647	68.701	45.773
PbO(s) red	0	-189.283	66.316	45.773
PbO ₂ (s)	-274.470	-215.396	71.797	61.119
Pb ₃ O ₄ (s)	-718.686	-601.606	211.961	154.933

Table A3. Physical Properties and Oxidation States of Co Oxides [42]

	Element	Formal oxidation state	MW(g)	Melting Point (°C)	Color	Density (kg/m ³)
Co	Co	0	58.9	1495	Metallic	8900
CoO	Co O	2 -2	74.9	1830	Grey or olive green	6400
Co ₃ O ₄	Co O	2,3 -2	240.8	900 (decomposes)	Black	6110

Table A2. Thermodynamic Properties of Co Oxides [43]

	ΔH_f° at 298.15 K (kJ/mol)	ΔG_f° at 298.15 K (kJ/mol)	S° at 298.15 K (J/mol K)	C_p at 298.15 K (J/mol K)
Co(s)	0	0	30.04	24.81
Co(g)	424.7	380.3	179.515	23.020
CoO(s)	-237.735	-213.988	52.993	55.279
Co ₃ O ₄ (s)	-910.020	-794.871	114.286	123.051

APPENDIX B

EQUILIBRIUM CONVERSION CALCULATIONS

App.B.1 Equilibrium Conversion Calculations For BaO

$$\Delta H_{rxn}^{\circ}(298.15\text{ K}, 1\text{ atm}) = \sum_i \nu_i \Delta H_{f,i}^{\circ}(298.15\text{ K}, 1\text{ atm})$$

$$\Delta G_{rxn}^{\circ}(298.15\text{ K}, 1\text{ atm}) = \sum_i \nu_i \Delta G_{f,i}^{\circ}(298.15\text{ K}, 1\text{ atm})$$

The storage reaction of Barium Oxide:



Table B.1 Thermodynamic Properties Species [36,37]

	ΔH_f° at 298.15 K (kJ/mol)	ΔG_f° at 298.15 K (kJ/mol)	S° at 298.15 K (J/mol K)
BaO	-558	-528	70.3
Ba(NO ₃) ₂	-992	-795	214
NO ₂	33.9	51.8	240
O ₂	0	0	205

$$\Delta H_{rxn}^{\circ} = (-992) - [2(33.9) + (-558)]$$

$$\Delta H_{rxn}^{\circ} = -501.8 \text{ kJ/mol}$$

$$\Delta G_{rxn}^{\circ} = -795 - [2(51.8) + (-528)]$$

$$\Delta G_{rxn}^{\circ} = -370.6 \text{ kJ/mol}$$

NO_x is 1000 ppm

O₂ is around 10 percent [38]



Table B2. Number of Moles for Species

Species	Initial Number of Moles	Final Number of Moles
NO ₂	0.001	0.001-2x
O ₂	0.1	0.1-(x/2)
Inert	0.899	-
TOTAL	1	0.101-5x/2

$$K_a(T) = \exp\left(-\frac{\Delta G_{\text{rxn}}^\circ}{RT}\right) = 9.17 * 10^{64}$$

Using relation between the equilibrium constant and the specific activities of species:

$$K_a(T) = \prod_{i=1} a_i^{v_i} = \frac{a_{\text{Ba}(\text{NO}_3)_2}}{a_{\text{NO}_2}^2 \times a_{\text{O}_2}^{1/2} \times a_{\text{BaO}}}$$

where $a_{\text{Ba}(\text{NO}_3)_2}$ and a_{BaO} are equal to 1 and it is assumed that:

$$a_{\text{O}_2} = C_{\text{O}_2}$$

$$a_{\text{NO}_2} = C_{\text{NO}_2}$$

$$K_a(T) = \frac{1}{\left[\frac{(0.1 - X/2)}{(0.101 - 5X/2)}\right]^{1/2} \left[\frac{(0.001 - 2X)}{(0.101 - 5X/2)}\right]^2}$$

$$K_a(T) = \frac{(0.101 - 5X/2)^{5/2}}{(0.1 - X/2)^{1/2} (0.001 - 2X)^2} = 9.17 * 10^{64}$$

X values are calculated according to the new K values evaluated for different temperatures (T=300-600 K) considering the following equation:

$$\ln[K_{eq}(T_2)/K_{eq}(T_1)] = -(\Delta H_{rxn}/R)*[(1/T_2)-(1/T_1)]$$

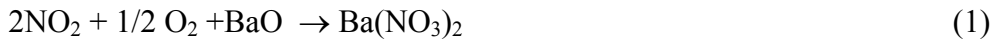
After evaluating the X values, conversions are calculated for each temperature.

App.B.2 Equilibrium Conversion Calculations For CoO

$$\Delta H_{rxn}^{\circ}(298.15\text{ K}, 1\text{ atm}) = \sum_i \nu_i \Delta H_{f,i}^{\circ}(298.15\text{ K}, 1\text{ atm})$$

$$\Delta G_{rxn}^{\circ}(298.15\text{ K}, 1\text{ atm}) = \sum_i \nu_i \Delta G_{f,i}^{\circ}(298.15\text{ K}, 1\text{ atm})$$

The storage reaction of Barium Oxide:



The storage reaction using Cobalt Oxide:



Table B.3 Thermodynamic Properties of Species [36,37]

	ΔH_f° at 298.15 K (kJ/mol)	ΔG_f° at 298.15 K (kJ/mol)	S° at 298.15 K (J/molK)
BaO	-558	-528	70.3
Ba(NO ₃) ₂	-992	-795	214
NO ₂	33.9	51.8	240
O ₂	0	0	205

For barium nitrate:

$$\Delta S = 214 - [2(240) + 1/2(205) + 70.3]$$

$$\Delta S_{rxn} = -438.8\text{ J/mol K}$$

$$= -0.4388\text{ kJ/mol K}$$

Table B.4 Thermodynamic Properties of Species [36,37]

	ΔH_f° at 298.15 K (kJ/mol)	ΔG_f° at 298.15 K (kJ/mol)	S° at 298.15 K (J/mol K)
CoO	-239	-213	43.9
Co(NO ₃) ₂	-420.5	Not available	Not available
NO ₂	33.9	51.8	240
O ₂	0	0	205

Since equations (1) and (2) are similar:

$$\Delta S_{\text{rxn}(1)} = \Delta S_{\text{rxn}(2)}$$

For cobalt nitrate:

$$-438.8 = S_{\text{Co}(\text{NO}_3)_2} - [2(240) + 1/2(205) + 43.9]$$

$$S_{\text{Co}(\text{NO}_3)_2} = 187.6 \text{ J/mol K}$$

$$\Delta H_{\text{rxn}}^0 = (-420.5) - [2(33.9) + (-239)]$$

$$\Delta H_{\text{rxn}}^0 = -249.3 \text{ kJ/mol}$$

$$\begin{aligned} \Delta G_{\text{rxn}}^0 &= \Delta G_{\text{Co}(\text{NO}_3)_2} - [-239 + 2(33.9)] \\ &= \Delta G_{\text{Co}(\text{NO}_3)_2} + 109.4 \end{aligned}$$

$$\Delta G = \Delta H - T\Delta S$$

$$\Delta G_{\text{Co}(\text{NO}_3)_2} + 109.4 = -249.3 - 298(-0.4388)$$

$$\Delta G_{\text{Co}(\text{NO}_3)_2} = -227.94 \text{ kJ/mol}$$

$$\Delta G_{\text{rxn}}^0 = -227.94 + 109.4 = -118.54 \text{ kJ/mol K}$$

NO_x is 1000 ppm

O₂ is around 10 percent [38].



Table B5. Number of Moles for Species

Species	Initial Number of Moles	Final Number of Moles
NO ₂	0.001	0.001-2x
O ₂	0.1	0.1-(x/2)
Inert	0.899	-
TOTAL	1	0.101-5x/2

$$K_a(T) = \exp\left(-\frac{\Delta G_{\text{rxn}}^\circ}{RT}\right) = 6.01 * 10^{20}$$

Using relation between the equilibrium constant and the specific activities of species:

$$K_a(T) = \prod_{i=1} a_i^{v_i} = \frac{a_{\text{Co}(\text{NO}_3)_2}}{a_{\text{NO}_2}^2 \times a_{\text{O}_2}^{1/2} \times a_{\text{CoO}}}$$

where $a_{\text{Co}(\text{NO}_3)_2}$ and a_{CoO} are equal to 1 and it is assumed that:

$$a_{\text{O}_2} = C_{\text{O}_2}$$

$$a_{\text{NO}_2} = C_{\text{NO}_2}$$

$$K_a(T) = \frac{1}{\left[\frac{(0.1 - X/2)}{(0.101 - 5X/2)}\right]^{1/2} \left[\frac{(0.001 - 2X)}{(0.101 - 5X/2)}\right]^2}$$

$$K_a(T) = \frac{(0.101 - 5X/2)^{5/2}}{(0.1 - X/2)^{1/2} (0.001 - 2X)^2} = 6.01 * 10^{20}$$

X values are calculated according to the new K values evaluated for different temperatures (T=300-600 K) considering the following equation:

$$\ln[K_{eq}(T_2)/K_{eq}(T_1)] = -(\Delta H_{rxn}/R)*[(1/T_2)-(1/T_1)]$$

After evaluating the X values, conversions are calculated for each temperature.

App.B.3 Equilibrium Conversion Calculations For PbO

$$\Delta H_{rxn}^{\circ}(298.15\text{ K}, 1\text{ atm}) = \sum_i \nu_i \Delta H_{f,i}^{\circ}(298.15\text{ K}, 1\text{ atm})$$

$$\Delta G_{rxn}^{\circ}(298.15\text{ K}, 1\text{ atm}) = \sum_i \nu_i \Delta G_{f,i}^{\circ}(298.15\text{ K}, 1\text{ atm})$$

The storage reaction of Barium Oxide:



The storage reaction using Lead Oxide:

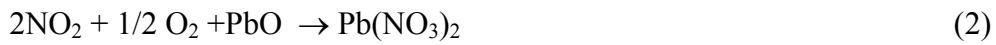


Table B.6 Thermodynamic Properties of Species [36,37]

	ΔH_f° at 298.15 K (kJ/mol)	ΔG_f° at 298.15 K (kJ/mol)	S° at 298.15 K (J/mol K)
BaO	-558	-528	70.3
Ba(NO ₃) ₂	-992	-795	214
NO ₂	33.9	51.8	240
O ₂	0	0	205

For barium nitrate:

$$\Delta S = 214 - [2(240) + 1/2(205) + 70.3]$$

$$\Delta S_{rxn} = -438.8\text{ J/mol K}$$

$$= -0.4388\text{ kJ/mol K}$$

Table B.7 Thermodynamic Properties of Species [36,37]

	ΔH_f° at 298.15 K (kJ/mol)	ΔG_f° at 298.15 K (kJ/mol)	S° at 298.15 K (J/mol K)
PbO	-218	-188	69.4
Pb(NO ₃) ₂	-449	Not available	Not available
NO ₂	33.9	51.8	240
O ₂	0	0	0

Since equations (1) and (2) are similar:

$$\Delta S_{\text{rxn}(1)} = \Delta S_{\text{rxn}(2)}$$

For lead nitrate:

$$-438.8 = S_{\text{Pb(NO}_3)_2} - [2(240) + 1/2(205) + 69.4]$$

$$S_{\text{Pb(NO}_3)_2} = 213.1 \text{ J/mol K}$$

$$\Delta H_{\text{rxn}}^0 = (-449) - [2(33.9) + (-218)]$$

$$\Delta H_{\text{rxn}}^0 = -298.8 \text{ kJ/mol}$$

$$\begin{aligned} \Delta G_{\text{rxn}}^0 &= \Delta G_{\text{Pb(NO}_3)_2} - [-188 + 2(51.8)] \\ &= \Delta G_{\text{Pb(NO}_3)_2} + 84.4 \end{aligned}$$

$$\Delta G = \Delta H - T\Delta S$$

$$\Delta G_{\text{Pb(NO}_3)_2} + 84.4 = -298.8 - 298(-0.4388)$$

$$\Delta G_{\text{Pb(NO}_3)_2} = -252.44 \text{ kJ/mol}$$

$$\Delta G_{\text{rxn}}^0 = -252.44 + 84.4 = -168.03 \text{ kJ/mol K}$$

NO_x is 1000 ppm

O₂ is around 10 percent [38]



Table B8. Number of Moles for Species

Species	Initial Number of Moles	Final Number of Moles
NO ₂	0.001	0.001-2x
O ₂	0.1	0.1-(x/2)
Inert	0.899	-
TOTAL	1	0.101-5x/2

$$K_a(T) = \exp\left(-\frac{\Delta G_{\text{rxn}}^\circ}{RT}\right) = 2.787 * 10^{29}$$

Using relation between the equilibrium constant and the specific activities of species:

$$K_a(T) = \prod_{i=1} a_i^{v_i} = \frac{a_{Pb(\text{NO}_3)_2}}{a_{\text{NO}_2}^2 \times a_{\text{O}_2}^{1/2} \times a_{PbO}}$$

where $a_{Pb(\text{NO}_3)_2}$ and a_{PbO} are equal to 1 and it is assumed that:

$$a_{\text{O}_2} = C_{\text{O}_2}$$

$$a_{\text{NO}_2} = C_{\text{NO}_2}$$

$$K_a(T) = \frac{1}{\left[\frac{(0.1 - X/2)}{(0.101 - 5X/2)}\right]^{1/2} \left[\frac{(0.001 - 2X)}{(0.101 - 5X/2)}\right]^2}$$

$$K_a(T) = \frac{(0.101 - 5X/2)^{5/2}}{(0.1 - X/2)^{1/2} (0.001 - 2X)^2} = 2.787 * 10^{29}$$

X values are calculated according to the new K values evaluated for different temperatures (T=300-600 K) considering the following equation:

$$\ln[K_{eq}(T_2)/K_{eq}(T_1)] = -(\Delta H_{rxn}/R)*[(1/T_2)-(1/T_1)]$$

After evaluating the X values, conversions are calculated for each temperature.

APPENDIX C

Co AND/OR Pb INCORPORATED SBA-15 SAMPLES SYNTHESIZED

Table C1. Co and/or Pb Incorporated SBA-15 samples at different weight loadings

Sample	Si wt%	Co wt%	Pb wt%	Intended Molar Ratios Si:Co:Pb
SBA-15	56	-	-	1:0:0
Co/SBA-15	40	40	-	1:0.476:0
	40	20	-	1:0.238:0
	40	15	-	1:0.178:0
	40	10	-	1:0.118:0
	40	5	-	1:0.0595:0
Pb/SBA-15	55	-	20	1:0:0.0493
	55	-	15	1:0:0.0369
	55	-	10	1:0:0.0246
	55	-	5	1:0:0.0123
Co-Pb/SBA-15	15	40	17	1:1.269:1.154
	15	20	17	1:0.635:0.154
	40	10	25	1:0.119:0.0842
	40	10	30	1:0.119:0.102

APPENDIX D

d-VALUES FOR THE METAL LOADED SAMPLES

Formula: PbO

Elements: Pb, O

JCPDS Card No: 76-1796

Table D1. d-values for Pb/SBA-15

d_{cal}	$I/I_{0\ cal}^*$	hkl	$d_{obs(A)}$
3.061	100	1 1 1	3.076
2.940	22	0 0 2	2.928
2.740	18	2 0 0	2.753
2.370	13	0 2 0	2.387
2.370	13	2 1 0	2.354
2.004	14	2 0 2	2.004
1.845	11	2 1 2	1.857
1.845	11	0 2 2	1.833
1.720	17	1 1 3	1.725
1.637	13	3 1 1	1.633
1.470	11	1 3 1	1.490
1.470	11	0 0 4	1.461

A: 20%Pb 55%Si

Table D2. d-values for Pb-Co/SBA-15

d_{cal}	I/I_0 cal*	hkl	$d_{obs(A)}$	$d_{obs(B)}$	$d_{obs(C)}$	$d_{obs(D)}$
3.061	100	1 1 1	3.066	3.051	3.076	3.066
2.940	22	0 0 2	2.905	2.947	2.938	2.938
2.740	18	2 0 0	2.744	2.728	2.748	2.720
2.370	13	0 2 0	2.378	2.372	2.381	2.357
2.370	13	2 1 0	2.369	2.351	2.372	2.351
2.004	14	2 0 2	2.013	1.998	2.011	2.006
1.845	11	2 1 2	1.856	1.852	1.836	1.850
1.845	11	0 2 2	1.847	1.849	1.825	1.842
1.720	17	1 1 3	1.729	1.726	1.723	1.710
1.637	13	3 1 1	1.635	1.638	1.639	1.634
1.470	11	1 3 1	1.477	1.476	1.478	1.469
1.470	11	0 0 4	1.469	1.473	1.464	1.462

A: 17%Pb 40%Co 15%Si, B: 17%Pb 20%Co 15%Si, C: 25%Pb 10%Co 40%Si, D: 30%Pb 10%Co 40%Si

(* Intensities $I/I_0 > 10\%$ are given.)

Formula: Co₃O₄

Elements: Co, O

JCPDS Card No: 78-1969

Table D3. d-values for Co/SBA-15

d _{cal}	I/I _{0 cal} *	Hkl	d _{obs(A)}	d _{obs(B)}	d _{obs(C)}	d _{obs(D)}	d _{obs(E)}
4.668	2	1 1 1	4.548	4.704	4.691	4.679	4.728
2.858	29	2 2 0	2.851	2.860	2.860	2.855	2.846
2.438	100	3 1 1	2.440	2.440	2.437	2.440	2.437
2.334	8	2 2 2	2.339	2.345	2.333	2.336	2.345
2.021	18	4 0 0	2.0256	2.023	2.021	2.0128	2.023
1.855	3	3 3 1	1.856	1.861	1.849	1.857	1.842
1.650	8	4 2 2	1.657	1.653	1.643	1.650	1.653
1.556	21	5 1 1	1.557	1.555	1.557	1.565	1.559
1.429	31	4 4 0	1.426	1.426	1.429	1.431	1.425
1.367	1	5 3 1	1.366	1.368	1.372	1.367	1.367
1.347	1	4 4 2	1.346	1.347	1.348	1.347	1.344
1.278	3	6 2 0	1.279	1.279	1.275	1.276	1.279

A: 40%Co 40%Si, B: 20%Co 40%Si, C: 15%Co 40%Si, D: 10%Co 40%Si, E: 5%Co 40%Si

Table D4. d-values for Pb-Co/SBA-15

d _{cal}	I/I _{0 cal} *	hkl	d _{obs(A)}	d _{obs(B)}	d _{obs(C)}	d _{obs(D)}
4.668	2	1 1 1	4.619	4.716	4.655	4.667
2.858	29	2 2 0	2.838	2.855	2.842	2.846
2.438	100	3 1 1	2.443	1.437	2.440	2.437
2.334	8	2 2 2	2.342	2.336	2.333	2.333
2.021	18	4 0 0	2.022	2.023	2.023	2.026
1.855	3	3 3 1	1.856	1.852	1.866	1.857
1.650	8	4 2 2	1.651	1.651	1.657	1.649
1.556	21	5 1 1	1.554	1.555	1.557	1.564
1.429	31	4 4 0	1.429	1.427	1.430	1.431
1.367	1	5 3 1	1.367	1.367	1.367	1.367
1.347	1	4 4 2	1.342	1.336	1.345	1.347
1.278	3	6 2 0	1.279	1.279	1.275	1.279

A: 17%Pb 40%Co 15%Si, B: 17%Pb 20%Co 15%Si, C: 25%Pb 10%Co 40%Si, D: 30%Pb 10%Co 40%Si

Formula: SiO₂

Elements: Si, O

JCPDS Card No: 44-1394

Table D5. d-values for Pb/SBA-15

d _{cal}	I/I _{0 cal} *	hkl	d _{obs(A)}	d _{obs(B)}	d _{obs(C)}	d _{obs(D)}
11.627	100	1 1 0	11.546	11.777	11.398	11.546
10.070	100	0 2 0	9.817	10.333	10.333	10.455
7.120	100	2 0 0	6.992	7.075	7.248	7.047
6.809	38	1 1 1	6.727	6.992	6.910	6.910
6.072	97	1 3 0	6.320	1.062	6.103	6.103
5.814	100	2 2 0	5.569	5.843	5.805	5.824
5.035	22	0 4 0	5.035	5.107	5.049	5.180
4.780	21	2 2 1	4.766	4.704	4.741	4.754
4.319	100	0 4 1	4.339	4.318	4.308	4.298
4.200	100	0 0 2	4.227	4.237	4.197	4.217
4.048	100	3 1 1	4.037	4.046	4.028	4.064
3.950	46	1 1 2	3.948	3.957	3.948	3.948
3.876	100	3 3 0	3.914	3.914	3.831	3.831
3.692	100	2 4 1	3.682	3.690	3.720	3.697
3.560	100	4 0 0	3.545	3.531	3.580	3.552
3.519	24	3 3 1	3.504	3.497	3.524	3.490
3.356	62	4 2 0	3.360	3.379	3.336	3.367
2.848	100	1 5 2	2.859	2.855	2.851	2.851
2.716	27	4 0 2	2.716	2.708	2.700	2.716
2.674	23	1 7 1	2.676	2.688	2.684	2.676
2.622	22	5 3 0	2.627	2.620	2.631	2.627
2.523	35	0 8 0	2.550	2.601	2.526	2.530
2.460	47	3 7 0	2.460	2.443	2.460	2.453
2.395	41	3 1 3	2.405	2.378	2.390	2.402
2.314	36	2 4 3	2.310	2.321	2.313	2.307
2.100	36	0 0 4	2.101	2.097	2.108	2.106
2.055	46	4 8 0	2.054	2.047	2.063	2.045
1.968	32	5 7 1	1.973	1.969	1.975	1.983
1.958	22	1 9 2	1.928	1.963	1.955	1.965
1.846	28	4 8 2	1.857	1.848	1.852	1.853
1.640	29	5 7 3	1.644	1.642	1.643	1.640
1.579	28	3 1 5	1.582	1.582	1.581	1.575
1.555	26	2 4 5	1.559	1.555	1.552	1.553

d_{cal}	$I/I_{0 cal}^*$	hkl	$d_{obs(A)}$	$d_{obs(B)}$	$d_{obs(C)}$	$d_{obs(D)}$
1.473	24	3 13 0	1.490	1.486	1.472	1.468
1.453	26	8 8 0	1.455	1.453	1.458	1.456
1.439	28	8 4 3	1.440	1.441	1.434	1.439
1.293	21	5 7 5	1.293	1.294	1.293	1.287

A: 20%Pb 55%Si, B: 15%Pb 55%Si, C: 10%Pb 55%Si, D: 5%Pb 55%Si

Table D6. d-values for Pb-Co/SBA-15

d_{cal}	$I/I_{0 cal}^*$	hkl	$d_{obs(A)}$	$d_{obs(B)}$	$d_{obs(C)}$	$d_{obs(D)}$
11.627	100	1 1 0	11.397	11.699	8.750	11.472
10.070	100	0 2 0	9.501	10.579	8.540	10.097
7.120	100	2 0 0	7.368	7.278	7.019	7.219
6.809	38	1 1 1	6.676	6.804	6.752	6.804
6.072	97	1 3 0	6.145	6.062	5.960	5.901
5.814	100	2 2 0	5.805	5.384	5.786	5.712
5.035	22	0 4 0	5.136	5.663	5.077	5.063
4.780	21	2 2 1	4.805	4.716	4.817	4.844
4.319	100	0 4 1	4.360	4.339	4.318	4.257
4.200	100	0 0 2	4.247	4.256	4.257	4.158
4.048	100	3 1 1	4.046	4.054	4.055	4.064
3.950	46	1 1 2	3.948	3.914	3.922	3.940
3.876	100	3 3 0	3.871	3.888	3.896	3.888
3.692	100	2 4 1	3.682	3.720	3.675	3.690
3.560	100	4 0 0	3.565	3.579	3.587	3.545
3.519	24	3 3 1	3.457	3.418	3.510	3.524
3.356	62	4 2 0	3.379	3.379	3.373	3.324
2.848	100	1 5 2	2.838	2.833	2.842	2.847
2.716	27	4 0 2	2.708	2.712	2.736	2.720
2.674	23	1 7 1	2.642	2.688	2.665	2.676
2.622	22	5 3 0	2.630	2.627	2.586	2.620
2.523	35	0 8 0	2.503	2.513	2.523	2.523
2.460	47	3 7 0	2.462	2.437	2.469	2.466
2.447	25	0 4 3	2.443	2.445	2.447	2.453
2.395	41	3 1 3	2.399	2.372	2.390	2.357
2.314	36	2 4 3	2.302	2.316	2.291	2.318
2.100	36	0 0 4	2.092	2.099	2.101	2.103
2.055	46	4 8 0	2.056	2.058	2.056	2.058
1.968	32	5 7 1	1.981	1.977	1.965	1.961
1.958	22	1 9 2	1.955	1.957	1.955	1.955

d_{cal}	$I/I_{0 cal}^*$	hkl	$d_{obs(A)}$	$d_{obs(B)}$	$d_{obs(C)}$	$d_{obs(D)}$
1.947	31	7 3 0	1.940	1.949	1.943	1.951
1.846	28	4 8 2	1.846	1.848	1.836	1.850
1.640	29	5 7 3	1.646	1.640	1.644	1.642
1.579	28	3 1 5	1.568	1.578	1.576	1.575
1.555	26	2 4 5	1.559	1.555	1.557	1.564
1.473	24	3 13 0	1.477	1.473	1.478	1.469
1.470	28	2 6 5	1.469	1.465	1.464	1.462
1.453	26	8 8 0	1.451	1.453	1.453	1.457
1.439	28	8 4 3	1.442	1.439	1.433	1.444
1.293	21	5 7 5	1.293	1.293	1.292	1.296

A: 17%Pb 40%Co 15%Si, B: 17%Pb 20%Co 15%Si, C: 25%Pb 10%Co 40%Si, D:
30%Pb 10%Co 40%Si

(* Intensities $I/I_0 > 20\%$ are given.)

APPENDIX E
TGA and DSC RESULTS

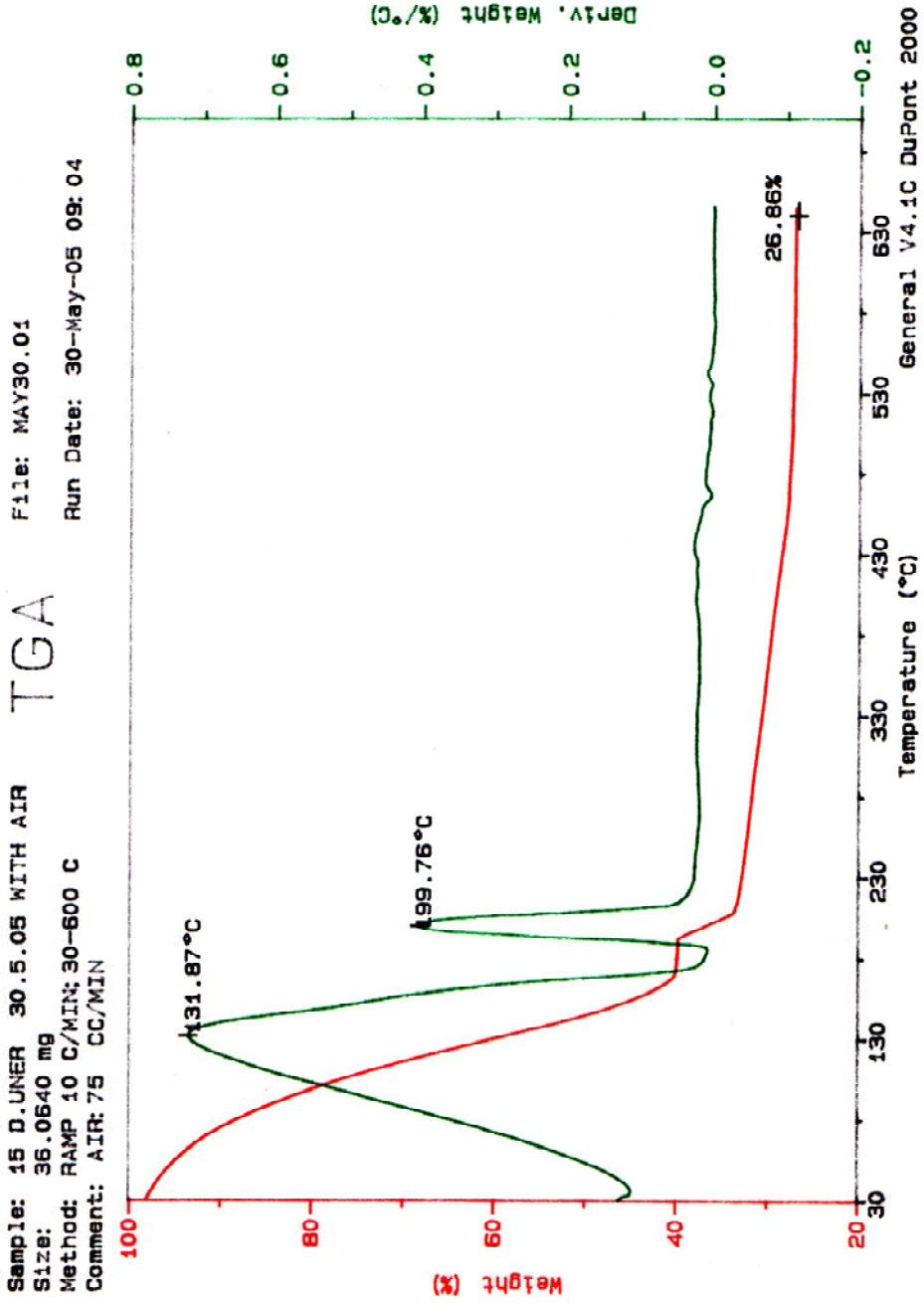


Figure E1. Thermo gravimetical analysis for 15%Pb 55%Si catalyst with Air

Sample: Co DENIZ UNER 2.5.05
Size: 5.2560 mg
Method: RAMP 5 C/MIN; 30-700 C
Comment: AIR: 50 CC/MIN

TGA

File: MAY2.01

Run Date: 2-May-05 08:32

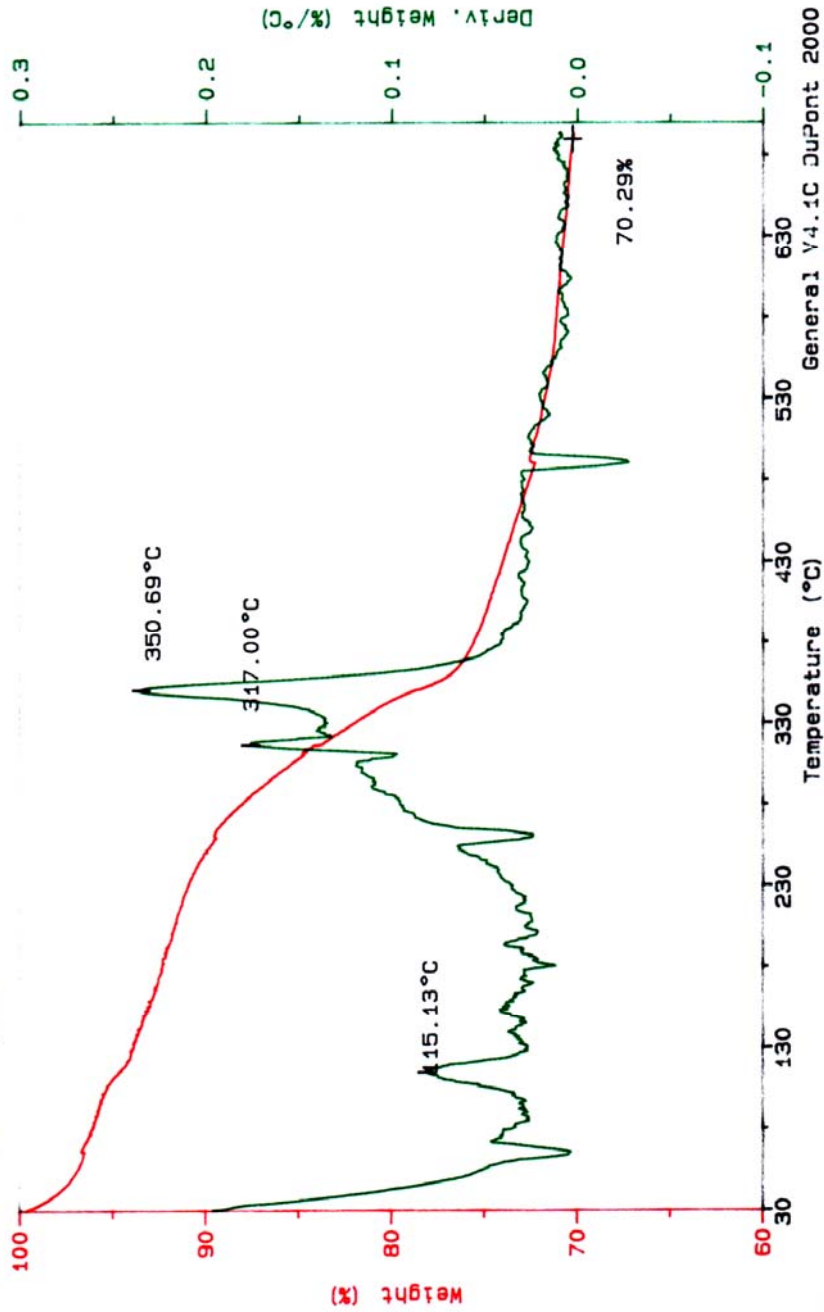


Figure E2. Thermo gravimetical analysis for 40%Co 40%Si catalyst with Air

Sample: 1 D.UNER 30.5.05 WITH AIR
Size: 46.0600 mg
Method: RAMP 10 C/MIN; 30-600 C
Comment: AIR: 75 CC/MIN

TGA

File: MAY30.02

Run Date: 30-May-05 11:09

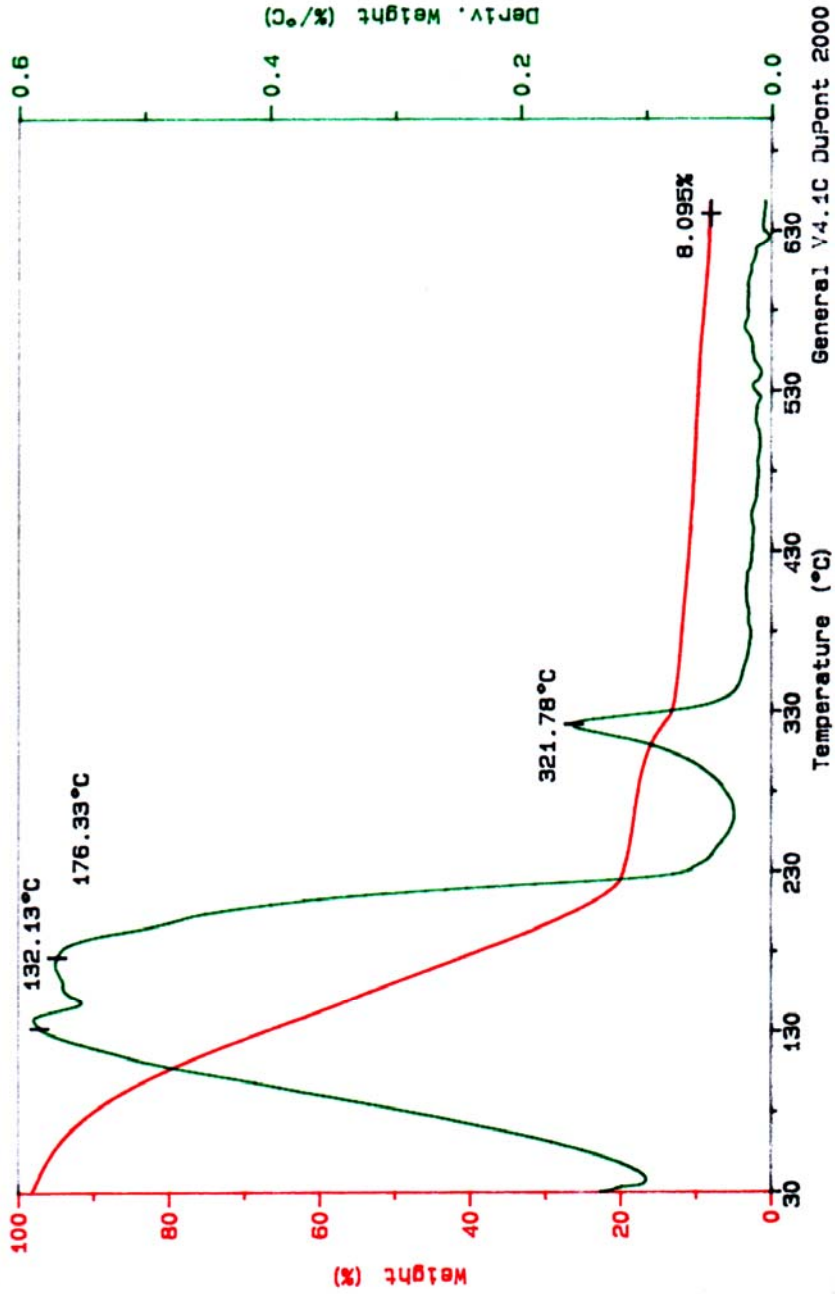


Figure E3. Thermo gravimetric analysis for 17%Pb 40%Co 40%Si catalyst with Air

Sample: 15XPb 7.6.05 D.UNER
Size: 25.0000 mg
Method: RAMP 5 C/MIN; 30-600 C
Comment: AIR: 75 CC/MIN

File: JUN7.01

DSC

Run Date: 7-Jun-05 09:23

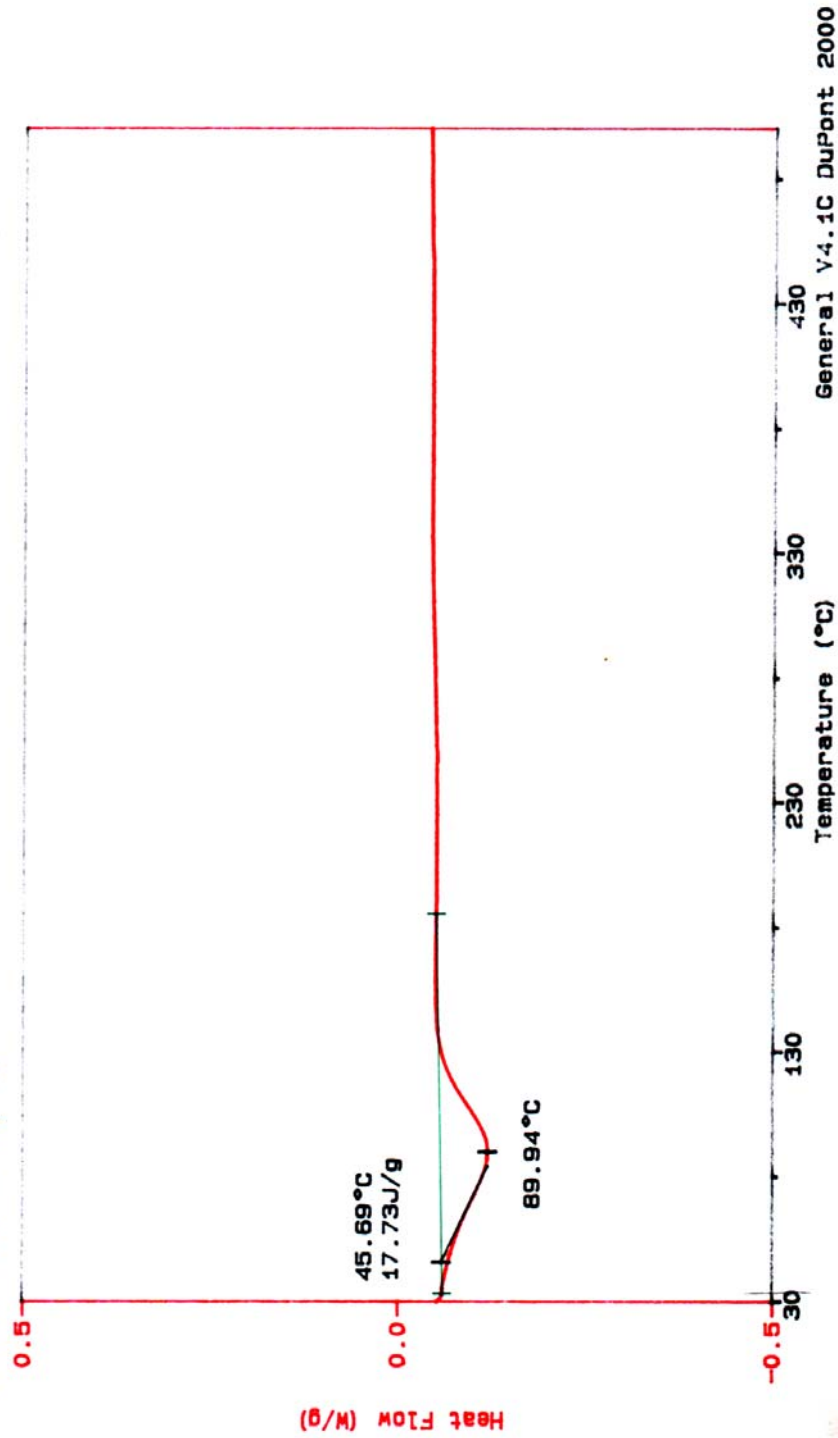


Figure E4. Differential Scanning Calorimeter Analysis of 15%Pb 55%Si catalyst with Air

Sample: Co DENIZ UNER 29.4.05
Size: 10.0000 mg
Method: RAMP 5 C/MIN; 30-500 C
Comment: AIR: 50 CC/MIN

DSC F11e: APR29.01

Run Date: 29-Apr-05 09:02

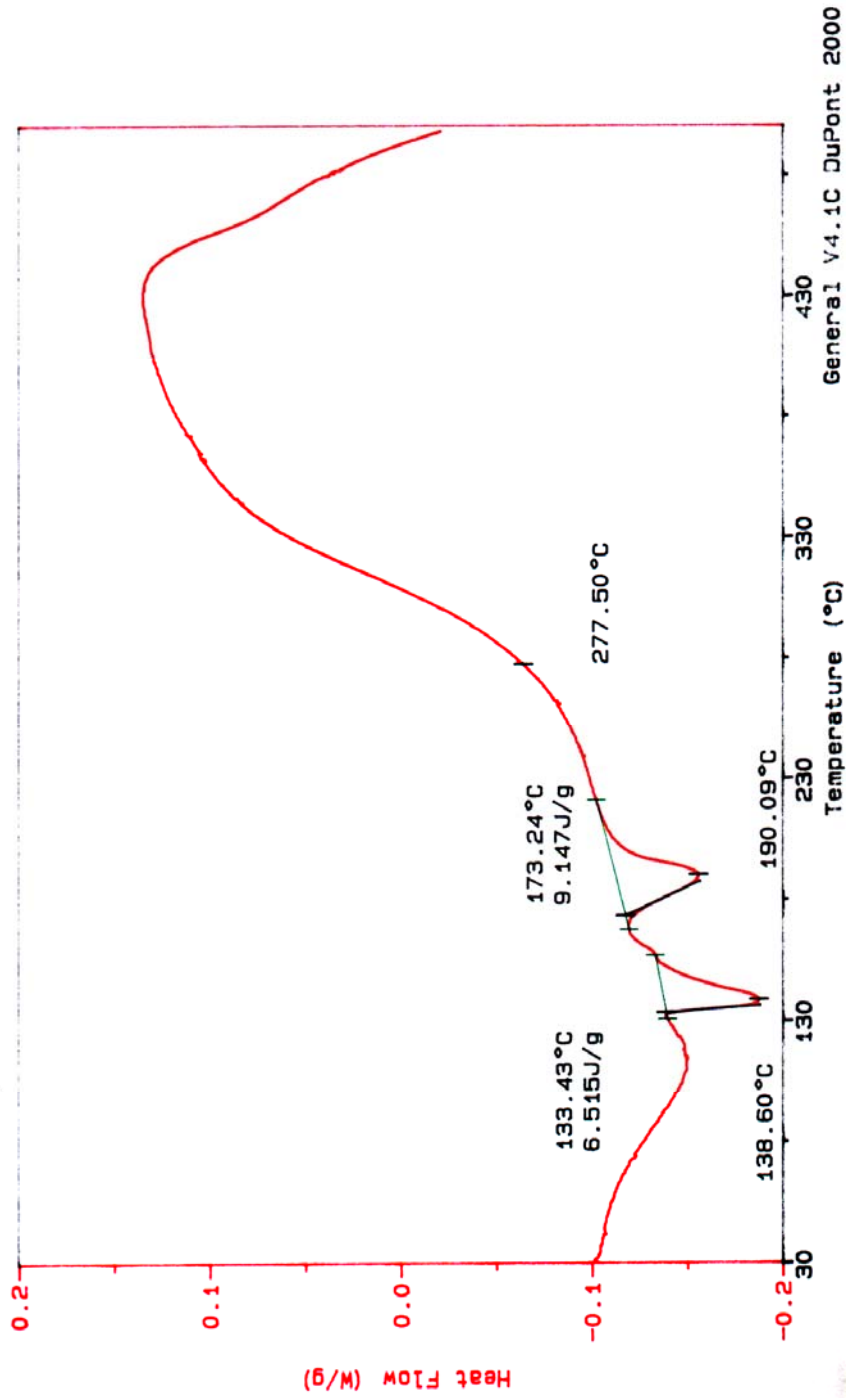


Figure E5. Differential Scanning Calorimeter Analysis of 40%Co 40%Si catalyst with Air

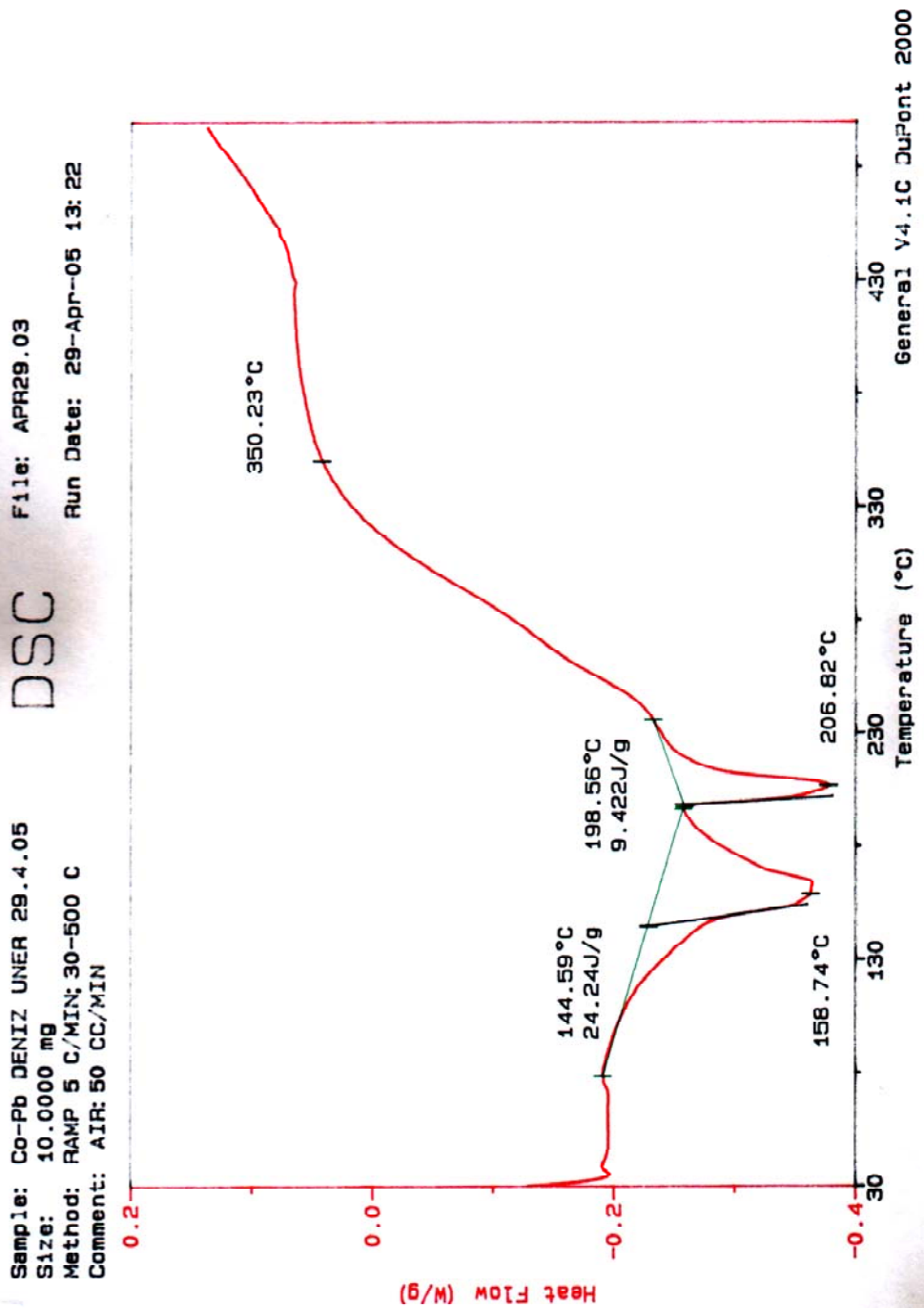


Figure E6. Differential Scanning Calorimeter Analysis of 17%Pb 40%Co 15%Si catalyst with Air